A&A 507, 327–345 (2009)
DOI: 10.1051/0004-6361/200912062

Astronomy & Astrophysics

C2D Spitzer-IRS spectra of disks around T Tauri stars

IV. Crystalline silicates⋆

J. Olofsson[1], J.-C. Augereau[1], E. F. van Dishoeck[2,3], B. Merín[4], F. Lahuis[5,2], J. Kessler-Silacci[6], C. P. Dullemond[7], I. Oliveira[2,12], G. A. Blake[8], A. C. A. Boogert[9], J. M. Brown[3], N. J. Evans II[6], V. Geers[10], C. Knez[11], J.-L. Monin[1], and K. Pontoppidan[12]

[1] Laboratoire d'Astrophysique de Grenoble, Université Joseph Fourier, CNRS, UMR 5571, Grenoble, France
e-mail: olofsson@obs.ujf-grenoble.fr
[2] Leiden Observatory, Leiden University, PO Box 9513, 2300 RA Leiden, The Netherlands
[3] Max Planck Institut für Extraterrestrische Physik, Giessenbachstrasse 1, 85748 Garching, Germany
[4] Herschel Science Centre, SRE-SDH, ESA PO Box 78, 28691 Villanueva de la Cañada, Madrid, Spain
[5] SRON Netherlands Institute for Space Research, PO Box 800, 9700 AV Groningen, The Netherlands
[6] The University of Texas at Austin, Department of Astronomy, 1 University Station C1400, Austin, Texas 787120259, USA
[7] Max Planck Institute for Astronomy, Königstuhl 17, 69117 Heidelberg, Germany
[8] Division of Geological and Planetary Sciences 150-21, California Institute of Technology, Pasadena, CA 91125, USA
[9] Infrared Processing and Analysis Center, MS 100-22, California Institute of Technology, Pasadena, CA 91125, USA
[10] Department of Astronomy and Astrophysics, University of Toronto, 50 St. George Street, Toronto, ON, M5S 3H4, Canada
[11] Department of Astronomy, University of Maryland, College Park, MD 20742, USA
[12] Division of Geological and Planetary Sciences 150-21, California Institute of Technology, Pasadena, CA 91125, USA

Received 13 March 2009 / Accepted 26 August 2009

ABSTRACT

Aims. Dust grains in the planet-forming regions around young stars are expected to be heavily processed due to coagulation, fragmentation, and crystallization. This paper focuses on the crystalline silicate dust grains in protoplanetary disks for a statistically significant number of TTauri stars (96).
Methods. As part of the cores to disks (c2d) legacy program, we obtained more than a hundred Spitzer/IRS spectra of TTauri stars, over a spectral range of 5−35 μm where many silicate amorphous and crystalline solid-state features are present. At these wavelengths, observations probe the upper layers of accretion disks up to distances of a dozen AU from the central object.
Results. More than 3/4 of our objects show at least one crystalline silicate emission feature that can be essentially attributed to Mg-rich silicates. The Fe-rich crystalline silicates are largely absent in the c2d IRS spectra. The strength and detection frequency of the crystalline features seen at $\lambda > 20$ μm correlate with each other, while they are largely uncorrelated with the observational properties of the amorphous silicate 10 μm feature. This supports the idea that the IRS spectra essentially probe two independent disk regions: a warm zone ($\lesssim$1 AU) emitting at $\lambda \sim 10$ μm and a much colder region emitting at $\lambda > 20$ μm ($\lesssim$10 AU). We identify a *crystallinity paradox*, as the long-wavelength ($\lambda > 20$ μm) crystalline silicate features are detected 3.5 times more frequently (~55% vs. ~15%) than the crystalline features arising from much warmer disk regions ($\lambda \sim 10$ μm). This suggests that the disk has an inhomogeneous dust composition within ~10 AU. The analysis of the shape and strength of both the amorphous 10 μm feature and the crystalline feature around 23 μm provides evidence for the prevalence of μm-sized (amorphous and crystalline) grains in upper layers of disks.
Conclusions. The abundant crystalline silicates found far from their presumed formation regions suggest efficient outward radial transport mechanisms in the disks around TTauri stars. The presence of μm-sized grains in disk atmospheres, despite the short timescales for settling to the midplane, suggests efficient (turbulent) vertical diffusion, probably accompanied by grain-grain fragmentation to balance the expected efficient growth. In this scenario, the depletion of submicron-sized grains in the upper layers of the disks points toward removal mechanisms such as stellar winds or radiation pressure.

Key words. stars: pre-main sequence – planetary systems: protoplanetary disks – circumstellar matter – infrared: stars – methods: statistical – techniques: spectroscopic

1. Introduction

The silicate dust grains that are originally incorporated into stellar nebulae and eventually constitute planet-forming disks are thought to have interstellar medium (ISM) size and composition, namely submicron in diameter and extremely amorphous (>99%) in structure (e.g. Gail 1998). Solar System comets, on the other hand, show high crystallinity fractions. The silicate grains in Oort comet Hale-Bopp are, for instance, composed of 40 to 60% of Mg-rich crystalline grains (Wooden et al. 1999, 2007; Crovisier et al. 1997), while Jupiter family comets have slightly lower crystalline fractions of about 25−35% (e.g. comet 9P/Tempel 1, Harker et al. 2007). Although the actual crystalline fraction may depend somewhat on the methodology used to calculate the dust's optical properties (e.g. Min et al. 2008), the clear detection of crystalline silicates features in comet spectra indicates that their mass fraction is high compared to the ISM. The amorphous silicate grains that were

⋆ Tables 4, 5 and Figs. 15–24 are only available in electronic form at http://www.aanda.org

incorporated into the Solar nebula must have been processed in the very early stages of planet formation before being incorporated into comets. Because of the high temperatures required to thermally anneal amorphous silicates and modify their lattice structure, it is generally accepted that the crystallization of amorphous silicates occurred close to the young Sun. The crystalline silicates were then transported outwards by processes such as turbulence or winds, leading to possible radial variations that may explain some of the mineralogic differences observed between small Solar System bodies today. Other processes could also explain the presence of crystals in the outer regions, such as shock waves triggered by gravitational instabilities in the solar nebula as described in Desch & Connolly (2002) and Harker & Desch (2002). Locally, such shocks could heat up enough surrounding materials to anneal and crystallize amorphous grains. In all these scenarios, silicate crystalline grains can be considered as tracers of the history of the protoplanetary, circumsolar disk.

The detection of silicates in the disks around young stars was notoriously difficult until the *Infrared Space Observatory* (ISO) and, later, the *Spitzer Space Telescope* were launched. Thanks to ISO, mid- to far-IR spectroscopy of disks around young intermediate mass stars (Herbig Ae/Be stars, hereafter, HAeBe) could be performed. Acke & van den Ancker (2004) showed that 52% of HAeBe stars exhibit emission in the 10 μm (amorphous) silicate feature that arises from the upper layers of the disks, while 23% of these stars show features at 11.3 μm, which is associated with forsterite, a Mg-rich crystalline silicate. Using the mid-IR capabilities of MIDI on the VLT Interferometer, van Boekel et al. (2004) spatially resolved the 10 μm emission zone for three HAeBe stars. They found a gradient of crystallinity, with a larger fraction of enstatite and forsterite crystalline grains located close to the star (1−2 AU) and lower fractions farther away in the disk (2−20 AU). This was among the first observations where the disk dust content was proven to be radially inhomogeneous.

Although TTauri stars were too faint for observations with the ISO/SWS and LWS, Natta et al. (2000) employed the lower spectral resolution ISOPHOT instrument to detect the broad amorphous silicate emission feature at around 10 μm for 9 stars in the Chameleon I cloud; but low resolution, low signal-to-noise ratios and limited spectral range did not allow firm detection of any crystalline features in the disks around young solar mass stars. Pioneering ground-based observations of TTauri stars (hereafter TTs) nevertheless showed evidence for forsterite emission features in the terrestrial spectral window around 10 μm. Honda et al. (2003), for example, clearly identified the presence of crystalline silicate emission features (forsterite at 10.1, 10.5 and 11.2 μm, and possibly enstatite at 10.9 μm) in the N-band spectrum ($R \sim 250$) of Hen 3-600A, and argued that the crystalline grains represent about 50% (30% enstatite, 20% forsterite) of the total mass of grains emitting at 10 μm. Because of the difficulty disentangling grain growth, emission from PAHs (Polycyclic Aromatic Hydrocarbon) or emission from forsterite as the main cause of the 11.3 μm "feature" in some disks (see e.g. Sitko et al. 2000; and the discussion in Przygodda et al. 2003), an unambiguous assessment of the presence of crystalline silicates in large samples of TTauri disks has awaited the launch of Spitzer.

The high sensitivity and large spectral range (5−35 μm) of the IRS spectroscopic instrument onboard Spitzer permits routine mid-infrared spectroscopy of TTauri disks in nearby molecular clouds. Surveys of young solar analogs in different star-forming regions such as those by Furlan et al. (2006) and Watson et al. (2009) for the Taurus cloud, and of amorphous silicate features in other clouds by Kessler-Silacci et al. (2006), were performed. Detailed mineralogic fits analysing the amorphous and crystalline silicate fractions in TTauri disks were performed by Bouwman et al. (2008, 7 TTs) and Sargent et al. (2009, 65 TTs), as well as for disks around much lower mass objects like the borderline brown dwarf (hereafter, BD) SST-Lup3-1 (Merín et al. 2007), and the BD 2MASS J04442713+2512164 in the Taurus cloud (Bouy et al. 2008), both of which show abundant crystalline silicate grains despite their low (sub-)stellar temperatures. According to Bouwman et al. (2008), the crystalline content of the inner regions of TTauri disks appear to be mostly dominated by enstatite silicates while the crystalline content of the outer region instead seems dominated by forsterite grains. Such data point toward an inhomogeneous dust content within the disks which could result from a radial dependence of crystallisation processes, or a difference in the initial conditions under which these crystals formed. The evolution of crystalline silicates has also been studied by Watson et al. (2009, 84 TTs), who find that within the same environmental conditions, the silicate crystalline mass fraction varies greatly, from none to nearly 100%. They find that 90% of the objects in their sample present crystalline features in the 10 μm region (either the 9.2 μm enstatite feature or the 11.3 μm forsterite feature). Regarding other crystalline features at longer wavelengths, they found that 50% of the objects surveyed had detectable crystalline features at ~33 μm. Also, no strong correlations between crystalline indices and stellar parameters have been found, suggesting that some mechanisms (e.g. X-ray emission, giant planets formation or migration) operate to erase the correlations that are expected from the standard models of crystallisation processes.

Here we present a comprehensive study of crystalline silicates in more than a hundred disks around young stars based on 5−35 μm IRS spectroscopic observations obtained as part of the c2d Spitzer legacy program from molecular clouds to planets (Evans et al. 2003). This work is the continuation of a series of c2d/IRS papers, studying grains, PAHs and gas in inner disk regions around young stellar objects (class II). Paper I by Kessler-Silacci et al. (2006) focuses on amorphous silicate features as a proxy for grain growth in a subsample of the c2d IRS class II objects. They find that the grain size is a function of spectral type. Paper II by Geers et al. (2006) shows evidence for low fractions of PAHs around TTs, indicating low gas phase PAHs abundance in disks as compared to the ISM. Paper III by Lahuis et al. (2007) reports the first detections of [Ne II] and [Fe I] gas-phase lines in TTauri disks.

In this paper, we present in Sect. 2 IRS observations of the entire c2d/IRS sample of class II objects, and we provide in Sect. 3 an overview of the detection statistics of solid-state emission features, especially those from crystalline silicates. In Sect. 4 we study the properties of crystalline silicate grains, including their size, and search for correlations between amorphous and crystalline silicates and between the SED shape and grain size. We further investigate the difference in crystallinity between the inner and outer regions of disks. In Sect. 5 we discuss the implications of our results for the dynamics of disks at planet-forming radii, and we summarize our results in Sect. 6. In a companion paper (Olofsson et al. 2009b, in prep.), we analyse in more detail the dust mineralogy based on compositional fitting of the complete spectra.

2. Spitzer/IRS observations

We present in this study the infrared spectra of disks around 108 young stellar objects obtained as part of the c2d Spitzer

legacy program. The spectra were obtained using the IRS instrument onboard the Spitzer Space Telescope. It was used to expand the early spectroscopic studies of HAeBe stars with ISO, and of a few TTs observed from the ground in the $\lambda \sim 10$ μm atmospheric window. Thanks to the high sensitivity of Spitzer, a large sample of disks around low-mass and solar-mass stars could be efficiently observed.

The IRS spectrograph is composed of four different modules that enable a wavelength coverage from 5 to 37 μm. Two modules, short-low and long-low (SL and LL hereafter), provide a spectral resolution between 60−127 over ranges of 5.2−14.5 μm and 14.0−38.0 μm for SL and LL, respectively. The remaining two modules, Short-High and Long-High (SH and LH hereafter), have a spectral resolution of about 600. They cover more limited spectral ranges of 9.9−19.6 μm and 18.7−37.2 μm for SH and LH, respectively.

2.1. Stellar sample

In this paper, we focus on class II objects – young stars no longer embedded in their protostellar envelope and surrounded by a circumstellar disk, where the dust may already be significantly processed. Our selection contains objects classified as class II according to the literature, but also 10 objects with no known spectral type. In this sample, 30 objects are sources newly discovered with the instrument IRAC onboard Spitzer as part of the mapping phase of the c2d project. All such objects are named with the prefix SSTc2d, and are classified as class II objects according to Evans et al. (2009) except for one source with no known classification (SSTc2d J182909.8+03446). The object SSTc2d J162221.0-230403 is characterized as class I, but shows amorphous 10 μm emission without additional absorption features. Two other SSTc2d objects have no classification. However, for the 10 objects with no classification in the literature, they were retained in the full list as they clearly show amorphous silicate features in emission.

The final sample contains 108 stars including 60 TTs, 9 HAeBe and 1 BD. The 38 remaining objects have no spectral classification in the literature, or are new SSTc2d stars discovered with Spitzer. This sample is distributed toward several clouds: Perseus (16 objects), Taurus (9), Chamaeleon (23), Ophiuchus (25), Lupus (16), Serpens (15), and includes 4 isolated stars: 3 HAeBes (BF Ori, HD 132947 and HD 135344) and one TT star (IRAS 08267-3336). All six clouds are young star-forming regions (1−5 Myr), located at distances within 140 and 260 pc from the Sun, with star densities (number of young stellar objects per square parsec) lying between 3 and 13. Some clouds are therefore quite extended, like Taurus or Lupus. The main cloud properties are given in Evans et al. (2009). The complete list of IRS targets analysed in this paper, their classifications and spectral types, as well as details about the observations, are given in Table 4.

Out of the 108 objects, four display spectra unusual for class II objects. These objects are DL Cha, HD 132947, SSTc2d J182849.4+00604 and SSTc2d J182859.5+03003. The first three sources all display spectra reminiscent of those observed toward Oxygen-rich Asymptotic Giant Branch stars (see Sloan et al. 2003, for example spectra) while the fourth object displays a spectrum similar to a C-rich AGB star. Both SSTc2d objects located in the Serpens cloud are objects newly discovered using Spitzer/IRAC surveys. DL Cha is a known variable star in Chamaeleon and HD 132947 is an isolated Herbig star, classified in the literature as a pre-main sequence star (see e.g. Valenti et al. 2003). We do not question here the classification of these four stars, but as they display unusual spectra (see Fig. 24), we decided to remove them from the rest of the study.

2.2. Data reduction

The spectra presented in this paper were extracted from S13 pre-reduced (BCD) data using the c2d legacy team pipeline (Lahuis et al. 2006) which uses two different extraction methods: full aperture extraction and optimal point spread function (PSF) extraction. The full aperture extraction method is applied to both low and high spectral resolution modules. For the low resolution modules, the c2d pipeline implements an extraction with a fixed-width aperture over the whole order. The source position in the slit is determined and the aperture is then centered on the source. The width is such that 99% of the flux of a point-source falls within the window. For the high resolution modules, the full slit width is used for the extraction. One disadvantage of this method is that the reduced spectra present a number of spikes (mainly due to bad pixels response, or "hot" pixels on the array, see below) that cannot be easily removed by automated pipelines.

For the PSF extraction, the observed signal is assumed to be that of a point source or slightly resolved source plus an uniform zero level. This zero level, in most cases, represents the local extended emission close to the source, and the typical PSF profile is calculated from high signal-to-noise ratio calibrator data. As this zero-level may also contain residuals from, for example, raw pipeline dark current, we remove this contribution. PSF fitting is less sensitive to bad data samples and unidentified bad pixels than the aperture extraction method. The *Spitzer Science Center* provides masks with known bad pixels, but they are not all identified. Our pipeline detects such remaining pixels. The LH array is particularly affected by this issue, but other modules require attention. With the PSF extraction method, bad pixels are simply eliminated, whereas their values are interpolated for the full aperture extraction method. The PSF extraction method, in addition, provides an estimate of the data zero level or sky contribution to the observed spectrum. An important disadvantage of the PSF fitting method, however, is that for some modules (mainly for the 2nd orders), the PSF is subpixel in size and the extraction method can become unstable. Thus, for some sources, the 2nd order of the SL module and the 2nd order of the LL module are unavailable, leading to incomplete spectra.

In this paper, we adopt the PSF extraction method in order to obtain spectra with as few spikes as possible. Where the PSF extraction method is not available or turns out to be unstable, we use the full aperture extraction method to build spectra. We then opt for a median filtering scheme to remove the remaining spikes: for the SL and SH modules we use a median smoothing over three channels while we use a median smoothing over five channels for the LL and LH modules. Some problems were encountered with the data reduction for two objects in our sample: EC69 and ISO-Cha237. For the latter source there are two possible explanations: either the LL1 module spectrum poorly matches the LL2 module spectrum, or the LL2 module pipeline reduction failed and its slope is off. The second explanation seems the most likely, given the shape of the red side of the 10 μm feature. For EC69, flux values for some orders were null. We decided to keep these two objects in our sample, first because ISO-Cha237 shows a 10 μm feature that can be analysed. For EC69, the spectrum appears featureless, and as it is classified as a TTauri star, we choose not to bias our results by removed "problematic" spectra.

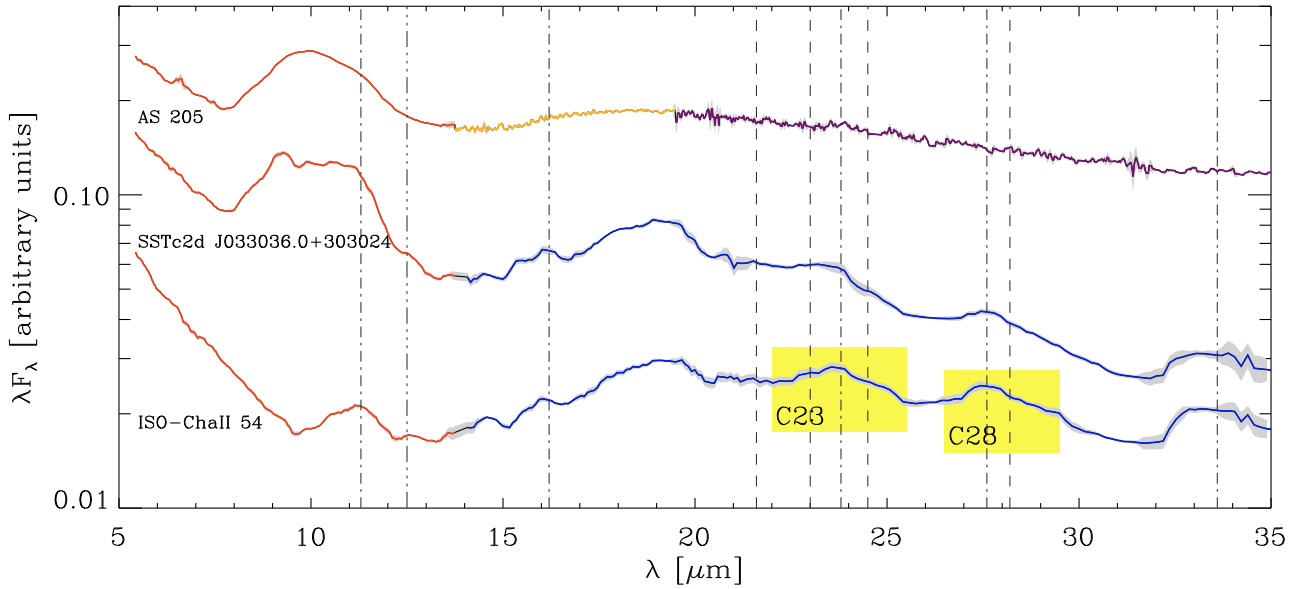

Fig. 1. Example Spitzer/IRS spectra of 3 T Tauri stars (top spectrum: SL+SH+LH modules, bottom spectrum: SL+LL). The grey envelopes correspond to 3-σ uncertainties as estimated in Sect. 2.4. The vertical lines show the peak positions of enstatite (dashed lines) and forsterite (dot-dashed lines) crystalline features that were searched for in every spectrum of our 108 star sample (see also Table 2). The 12.5 μm feature (triple-dot dashed line) is attributed to silica, and the two yellow boxes correspond to the C23 and C28 crystalline complexes discussed in Sect. 3.1.1.

Table 1. Overview of the modules used to obtain the final spectra.

Case	SL1	SL2	SH	LL1	LL2	LH	Number of stars
0	–	–	√	–	–	√	9
1	–	–	√	√	–	√	2
2	√	√	–	√	√	–	51
3	√	√	√	–	–	√	18
4	√	√	√	√	–	√	22
5	√	√	√	√	√	–	6

Note: SL1: 7.4–14.5 μm, SL2: 5.2–7.7 μm, LL1: 19.5–38.0 μm, LL2: 14.0–21.3 μm.

2.3. Module merging and offset correction

The c2d pipeline corrects for telescope pointing errors that may lead to important flux offsets between the different modules. Some small offsets can nevertheless remain between modules even after pointing correction, and an additionnal post-processing offset correction is thus applied. This correction depends on the modules available for every spectrum. Table 1 gives a summary of all the possible configurations, and list the modules used in all the cases we encountered to obtain the final spectra. The exact modules used for each individual star are given in Table 4. A tick-mark (√) means that data provided by this module are used to build the final spectrum. Priority was given to SL and LL, first because the spectral resolution is sufficient for detecting crystalline features, and second, because the high resolution modules provide noisier spectra than those from the low resolution modules. For each star, a final spectrum is then obtained by merging all the chosen modules and correcting manually for small remaining offsets. The spectra themselves are presented in Figs. 1, 2 and 15–23.

2.4. Estimating the uncertainties

The uncertainties propagated through the c2d pipeline are dominated by the flux calibration error estimates. As our study is oriented toward the detection of features in emission from silicates, we are only concerned with relative uncertainties which are evaluated by dividing the original spectrum by a smoothed version of itself obtained using a Savitzky-Golay filter (Savitzky & Golay 1964). This provides an estimate of the signal-to-noise ratio (*SNR*) on the spectrum, and is used to assess the presence of features as follows: the Savitzky-Golay filtering process calculates a local 3rd-order polynomial for every point of the spectrum, based on the four left and right neighbors. The main advantage of this filter is that it maintains the shape and contrast of the features, while "pointy" features tend to be rounded out with classical average smoothing, thereby increasing the uncertainties at the top of every feature and downgrading the actual quality of the data. The Savitzky-Golay filter has only been used to calculate the uncertainties displayed as grey envelopes in Figs. 1, 2 and 15–23, not affecting the spectra themselves presented in these figures and used for the scientific analysis.

3. Overview of observed solid-state features

3.1. Observed crystalline silicates

The 104 spectra analysed in this paper are displayed in Figs. 15 to 23, for wavelengths between 5 and 35 μm and in units of Jy (F_ν). They are sorted by cloud and increasing Right Ascension. The spectra of the four isolated stars in our sample are displayed in Fig. 23.

Broad emission features at 10 and 20 μm from amorphous silicates can be identified in many spectra, as well as narrower emission features. The latter are identified more easily beyond 20 μm, and are due to crystalline silicates. Figure 1 illustrates the diversity of the spectra seen in our sample. ISO-ChaII 54 (bottom spectrum) shows many crystalline features, with a weak 10 μm band. In contrast, AS 205 (top spectrum) is almost "pristine", with strong amorphous bands and

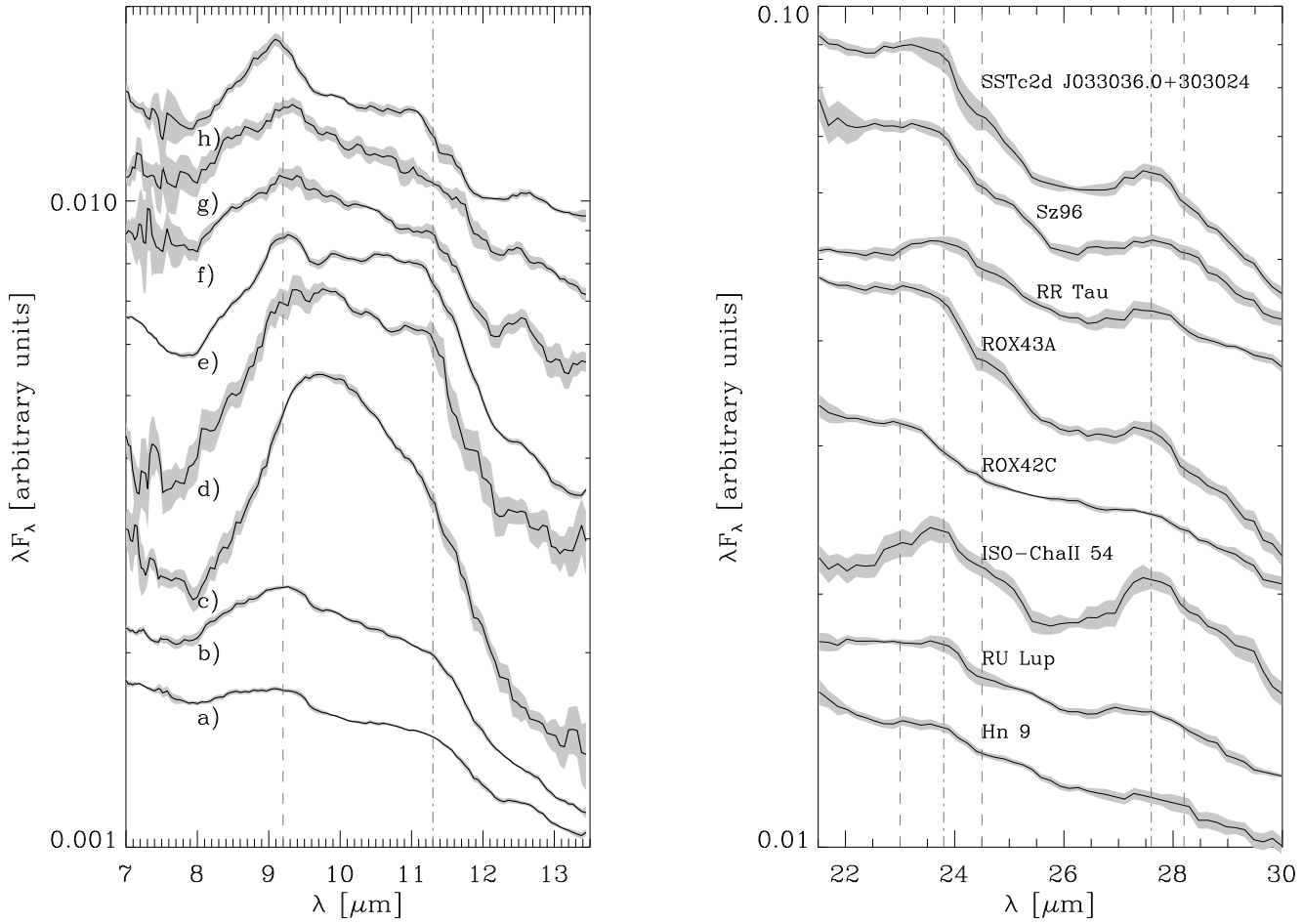

Fig. 2. *Left panel*: examples of the 9.2 (enstatite), 11.3 (forsterite) and 12.5 μm (silica) features superposed on the amorphous 10 μm feature. *Right panel*: examples of the C23 and C28 crystalline silicate complexes. The grey areas correspond to 3-σ uncertainties. Dashed lines correspond to enstatite emission features, dot-dashed lines correspond to forsterite emission features. The sources in *the left panel* are **a)** Wa Oph 6, **b)** LkHα 325, **c)** TW Cha, **d)** SSTc2d J161159.8-382338, **e)** SSTc2d J033036.0+303024, **f)** Sz52, **g)** XX Cha and **h)** ROX42C.

no evidence of crystalline features[1]. The third spectrum, for SSTc2d J033036.0+303024, has both amorphous and crystalline features. The crystalline features in disks can, in most cases, be attributed to Mg-rich silicate minerals (with a possible contribution from Ca-rich silicates); in agreement with some model predictions (e.g. Gail 2004, and reference therein), and as observed in solar system comets (e.g. Wooden et al. 2007).

3.1.1. Mg-rich crystalline silicates: forsterite and enstatite

Table 2 presents the different crystalline silicate features we searched for in every spectrum – in addition to the amorphous silicate feature at 10 μm. In Table 2, "Peak λ" is taken from the literature, "Measured λ" and "$\Delta\lambda$" values are the peak positions and equivalent widths measured by our observations. "C23" and "C28" refer to silicate features blended in complexes. Uncertainties are standard deviations. Here we consider features arising from Mg-rich silicates, specifically enstatite (inosilicate belonging to the pyroxene group, with chemical formula $MgSiO_3$) and forsterite, the nesosilicate Mg-rich end-member of the olivine group (Mg_2SiO_4). Blowups of representative spectral features are shown in Fig. 2. Using IRS spectra, we cannot disentangle differences between crystalline structures, for instance, clino-enstatite or ortho-enstatite. Still, according to Koike et al. (2000), enstatite features are most likely attributed to ortho-enstatite.

The example spectrum for ISO-ChaII 54, displayed in Fig. 1 as well as the blowups in the right panel of Fig. 2, shows that

[1] Extensive, narrow features not discussed in this paper, but seen between 10 and 20 μm in Fig. 1 are attributed to water emission lines (Salyk et al. 2008).

Table 2. Summary of the different crystalline silicate features examined in this study.

Crystal	Peak λ [μm]	Measured peak λ [μm]	Measured $\Delta\lambda$ Eq. width [μm]
Enstatite ($MgSiO_3$)	9.2[(1,2)]	9.24 ± 0.08	0.49 ± 0.11
	21.6[(1)]	21.47 ± 0.16	0.45 ± 0.25
	23.0[(1,2)]	C23	C23
	24.5[(1,2)]	C23	C23
	28.2[(1,2)]	C28	C28
Forsterite (Mg_2SiO_4)	11.3[(2)]	11.26 ± 0.12	0.60 ± 0.33
	16.2[(2)]	16.08 ± 0.16	0.38 ± 0.16
	23.8[(2)]	C23	C23
	27.6[(2)]	C28	C28
	33.6[(2)]	33.1 ± 0.63	1.19 ± 0.47
Diopside ($CaMgSi_2O_6$)	25.0[(2)]	25.14 ± 0.18	0.58 ± 0.22

References: [(1)] Koike et al. (2000); [(2)] Molster et al. (2002).

the 23.0, 24.5 μm enstatite and the 23.8 μm forsterite features can be blended into one single complex. Similarly, the 27.6 μm forsterite feature can also be blended with the 28.2 μm enstatite feature. In the following, we will treat these features as two complexes, at reference positions of 23 and 28 μm, independent of the actual crystals responsible for the observed emission. We shall note these two complexes, C23 and C28, which are by far the most frequently detected crystalline features in disks (Sect. 3.2.1). Figure 2 displays eight example spectra of the C23 and C28 complexes. Clearly, the shape and peak positions may vary from one object to another. We will show in Sect. 4.1 that some of these differences may relate to the mean size of the emitting grains, although the composition (more or less enstatite compared to forsterite), grain shape, and strength of the continuum might also contribute to the diversity of the C23 and C28 features observed.

Beside the features listed in Table 2, other enstatite bands at 10.6, 11.7 and 19.6 μm, as well as forsterite features at 10.1 and 19.7 μm were also searched for with little success in a subsample of 47 high *SNR* spectra. The detection rate of these crystalline features is very low and not significant. For the two enstatite and forsterite features at ~19.6 and 19.7 μm, the main difficulty lies in the added noise where SH and LH modules merge, which prevents any firm detection of these two features.

3.1.2. Fe-rich components: troilite and fayalite

The formation of Mg-rich crystalline silicates by direct condensation from a gas of solar composition (as opposed to formation by thermal annealing) is expected to additionally yield iron-bearing condensates, in particular FeS (or troilite, see Wooden et al. 2007). This condensate is of great interest and, while a detailed study of the ISO spectra of two HAeBe stars (including HD 163296, Fig. 18) carried out by Keller et al. (2002) indicates FeS in these systems, it remains difficult to detect, in general, because the main feature (between 17−26 μm), centered at 23.5 μm, is broad, and falls in a region where the IRS spectra are often noisy (due to module merging around 20 μm). Further, the disk spectra are often dominated by the presence of the 18 μm amorphous silicate feature as well as by frequent C23 emission features. Therefore, studying the presence or absence of FeS emission in the c2d sample is beyond the scope of this paper.

Another Fe-rich component that can potentially be detected in IRS spectra is fayalite, a crystal belonging to the olivine class (Fe_2SiO_4). Theoretical opacities from Fabian et al. (2001) show strong emission features around 30 μm. For small grains, three narrow features are expected at ~27, 29.3 and 31.6 μm. We find there are 4 objects where fayalite may tentatively be present, all four in the Chameleon cloud (Fig. 17): TW Cha, VZ Cha, WX Cha, and Sz62. Interestingly, the Sz62 spectrum also shows other features that can be attributed to fayalite, at roughly 11 μm and 19 μm. All these objects notably display a feature centered at around 30.5 μm, which is at shorter wavelength compared to the feature from pure fayalite which lies at 31.6 μm (e.g. Fabian et al. 2001; or Koike et al. 2003). This may reflect a small departure from pure Fe-rich crystalline olivine (e.g. ~10−15% Mg fraction) as illustrated by the three top spectra in Fig. 1 from Koike et al. (2003) where it is seen that the feature shifts to smaller wavelengths with increasing Mg-content. We note that there are other spectra that show some similar behaviours in the 30 μm region, but they are of lower signal-to-noise ratio and contain possible data reduction artifacts (see e.g. RX J0432.8+1735 spectrum, Fig. 16). These factors make it difficult to conclude whether fayalite is present or not. Because of the small number of positive detections and because of the ambiguity between possible noise and real features, we will not investigate the presence of this component further. We do note, however, that the compositional fits to seven Spitzer/IRS spectra of TTs by Bouwman et al. (2008) show no evidence of Fe-rich materials.

However, the previous conclusion means that we do not observe pure fayalite in our spectra. Considering the following formula for crystalline olivine $(Mg_xFe_{1-x})_2SiO_4$ (with $0 \leq x \leq 1$), features in the 20−30 μm spectral range become weaker (especially around 23 μm) for Mg fractions below 0.6. This means that we are actually probing crystalline olivine with at least more than 60% of Mg compared to Fe. Still, as crystalline pyroxene is also contributing to C23 and C28 complexes, further interpretations remain difficult.

3.1.3. Other silicates: diopside and silica

Diopside, a calcium magnesium silicate, and a member of the pyroxene group ($CaMg(SiO_3)_2$), can be searched for at ~25 μm. Because of the presence of the C23 complex, however, the diopside feature can sometimes be blended with the complex. Even worse, the shoulder of the complex can be mis-interpreted as a 25 μm feature. We therefore obtain only a lower limit on the frequency at which this feature is present. The low detection rate of an additional (but weaker) 20.6 μm diopside feature does not strengthen the confidence level of the detection of diopside in TTauri star disks.

Finally, silica (SiO_2) has also been identified in our spectra, with a feature arising at 12.5 μm. Attribution of this single feature to amorphous or crystalline silica is not straightforward. Sargent et al. (2009) showed that amorphous silica tends to produce a feature around 12.3−12.4 μm, while various crystalline silica polymorphs produce a feature centered at or slightly longward of 12.5 μm. Due to the presence of the broad amorphous 10 μm feature, disentangling the different contributions is beyond the scope of our statistical study of the most prominent crystalline silicates. Example silica features are shown in Fig. 1 and the left panel of Fig. 2.

3.2. Silicate feature statistics for TTauri stars

3.2.1. The fraction of disks showing silicate(s) feature(s)

We developed a routine that measures the characteristics of both crystalline and amorphous (10 μm) features. For each feature, it assumes a local continuum which is built using a two point Lagrange polynomial joining the feet of the feature, computed as follows:

$$F_{\nu,\mathrm{c}} = F_{\nu_1} \times \left(\frac{\lambda - \lambda_2}{\lambda_1 - \lambda_2}\right) + F_{\nu_2} \times \left(\frac{\lambda - \lambda_1}{\lambda_2 - \lambda_1}\right),$$

where $F_{\nu,\mathrm{c}}$ is the final continuum, λ_1 and λ_2 the blue and red feet of the feature, respectively, and F_{ν_1} and F_{ν_2}, the observed fluxes at λ_1 and λ_2, respectively. This routine returns the band flux, its peak position, the mean wavelength and the peak flux. It also returns the 1-σ uncertainty on the band flux. The results given by this procedure are presented in Table 5, in the form of the *SNR* on the measured feature fluxes using the above procedure. Results for only 101 objects out of total 104 are shown since 3 of them (2.8% of total sample) do not display any crystalline or amorphous silicate features. Those objects are: EC 69, EC 92 and Sz 84.

Thus, the overwhelming majority (~97%) of the disks do show at least one feature that can be attributed to silicates. Since 10 μm-sized or larger grains are essentially featureless in the IRS spectral range (see, for example, the theoretical opacities in Fig. 9), our results indicate qualitatively that inner disk atmospheres are populated by grains a few micrometers or less in size, independent of the age of our stars, and of cloud membership. Some differences between clouds are nevertheless addressed in Sect. 3.2.2, and a discussion concerning the size of the amorphous and crystalline silicate grains can be found in Sect. 4.1.

In the following, we remove the 8 HAeBe stars (plus HD 132947 that we already removed) in our survey from the statistical analysis so that the sample is composed mainly of objects classified as TTs. The statistics in the paper are therefore made on the remaining 96 objects.

3.2.2. The prevalence of crystalline features

Feature-by-feature statistics are displayed in Fig. 3, which shows detection fractions of crystalline features ranging between ~10% and ~60%. A visual inspection of the 28−29 μm and 33−35 μm features for a subset (40 TTs and 7 HAeBes) of the target sample analysed in this paper led Kessler-Silacci et al. (2006) to conclude that ~50% of the spectra show crystalline silicate features. Considering here the full 96 star sample and only secure detections with $SNR > 20$ for the C28 and 33.6 μm complexes, we obtain a fraction of ~65% (63 out of 96) for objects displaying at least one of the two features. Including all the other crystalline features (still with $SNR > 20$), this fraction rises to ~78% (75 out of 96 stars). We have checked that these results are not corrupted with possible PAH emission features, and that the 11.3 μm can be associated with forsterite. Indeed, Geers et al. (2006) identified only three objects in our sample that have potential PAHs emission at 11.3 μm: LkHα 330, T Cha and SR 21. All the other objects cited in Geers et al. (2006) are HAeBe stars and, therefore, not considered in our sample. With additional data, Geers (2007) could confirm the presence of PAHs for LkHα 330, T Cha and SR 21, and so these three objects have then been removed from our statistics for the analysis of the 11.3 μm forsterite feature. One other object, EC 82 is identified by Geers (2007) to have a 6.2 μm PAH feature but with no 11.3 μm counterpart, thereby avoiding any possible contamination in this particular case. Note that we have been as conservative as possible in identifying features, especially for the crystalline features around 10 μm. Some spectra display a shoulder at around 11.3 μm that could possibly be interpreted as a forsterite feature (see e.g. Sz 52 spectrum, Fig. 2, label *f*). We choose not to attribute such a shoulder to forsterite. Therefore, we conclude from our analysis that about 3/4 of the protoplanetary disks in our sample of young solar-analogs show at least one crystalline feature in their 5−35 μm spectrum, meaning that dust crystallization is not a marginal process but is instead widespread at this stage of disk evolution.

It is interesting to compare these results to those of Watson et al. (2009) who analysed 84 TTs in the Taurus-Auriga association, also using Spitzer/IRS. Developing indices measuring the departure from an ISM-like pristine 10 μm feature, they found that 90% of the Taurus-Auriga disks show either the 9.2 μm enstatite feature or the 11.3 μm forsterite feature, while we obtain about 20% for both features (Fig. 3). In Watson et al. (2009), any departure from the 10 μm pristine reference spectrum is considered as being evidence for crystalline features, while we argue that this frequent departure that we also observe has more to do with a grain size effect (see Sects. 4.1 and 5.3 for further discussions). There is therefore a difference in the interpretation of the measurements that leads to inconsistent conclusions. Watson et al. (2009) used the D'Alessio et al. (2006) model to investigate the impact of dust sedimentation on the observed dispersion in equivalent width for the 10 μm amorphous feature. They could reproduce a broad range of observed equivalent widths by depleting the dust fraction (that consists of grains ≤0.25 μm in their model) in the upper layers of the disks, thereby mimicking dust settling. In a more recent paper, Dullemond & Dominik (2008) find that sedimentation has a very limited effect on the shape of the 10 μm feature as long as a continuous grain size distribution is considered (as opposed to fixed grain sizes). For longer wavelength crystalline features, comparison with the work of Watson et al. (2009) is possible for the 33.6 μm forsterite feature, but not for the features around 23 and 28 μm as they did not study these two complexes. They find that 50% of the Taurus-Auriga objects show the 33.6 μm crystalline feature, compared to 28% for our sample, but this detection statistic is consistent with the statistics for the C23 (55%) and C28 (54%) crystalline complexes.

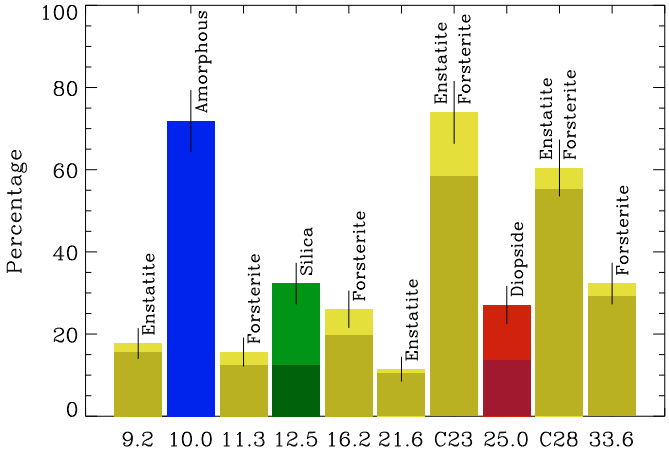

Fig. 3. Detection statistics for crystalline silicate features (yellow and red bars) for the 10.0 μm amorphous silicate feature (blue) and for silica at 12.5 μm (green). Darker color bars are positive detections ($SNR >$ 20), and lighter color bars stand for tentative detections ($SNR \leq 20$). The uncertainties are those due to Poisson statistics.

Figure 4 shows feature-by-feature statistics sorted by clouds. The largest occurrence of the C23 complex is found in the Ophiuchus cloud with about 80% of the objects showing this feature. Disks in Serpens have a prevalence of crystalline features significantly smaller than in the Perseus, Chamaeleon, Ophiuchus and Lupus clouds which show comparable fractions of amorphous and crystalline features. The Taurus cloud shows a noticeably low frequency of the 10 μm amorphous feature compared to the other clouds and does not appear to be balanced by a remarkably high fraction of crystalline grains when compared to the other regions. Our sample contains only eight objects in the Taurus cloud, however, which introduces a strong bias. Watson et al. (2009) found that the amorphous 10 μm feature is present for a large majority of the objects in their survey of 84 TTs. Therefore, discussing the differences is not statistically significant for our Taurus sample. One can notice that, except for Taurus, the five remaining clouds show very similar behavior. This points toward a rather homogeneous distribution of amorphous and crystalline silicate dust grains in disks throughout clouds. Detection statistics in the Serpens cloud are overall smaller, but the trends are the same as that in the other clouds. Our current result on the Serpens cloud will be revisited in a

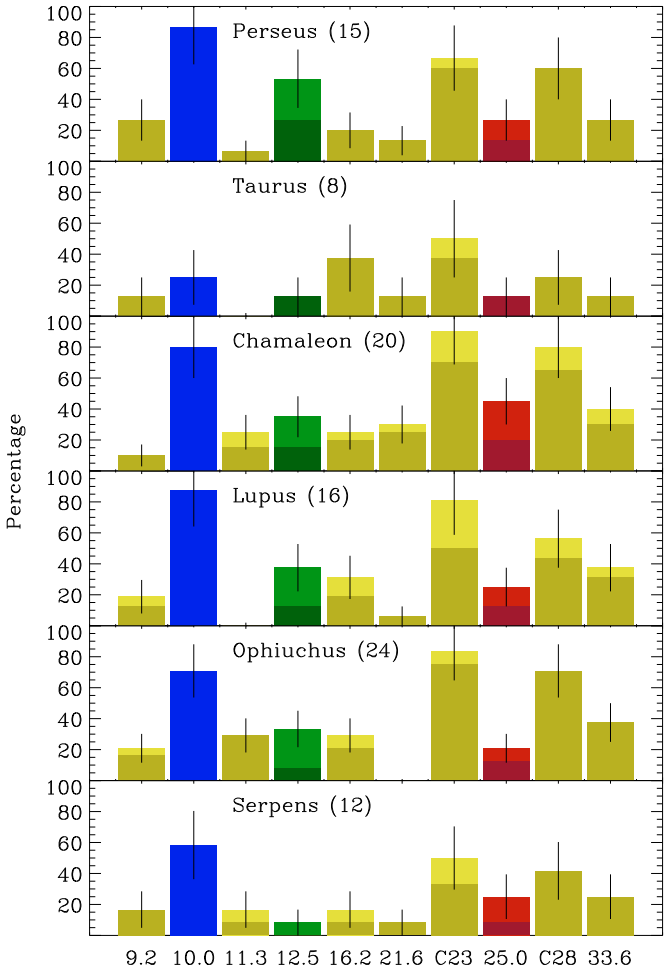

Fig. 4. Same as Fig. 3 but now sorted by clouds. Uncertainties are again Poisson noise, derived from the number of objects per cloud: 15 for Perseus, 8 for Taurus, 20 for Chamaeleon, 16 for Lupus, 24 for Ophiuchus and 12 for Serpens.

forthcoming paper by Oliveira et al. (in prep.) who analyse a much larger sample of more than a hundred Serpens objects observed with Spitzer/IRS.

In the following, we will treat all the objects as a single sample. The first reason for this is that cloud-to-cloud differences suffer from low statistics and merging the entire sample will increase the significance of our inferences (96 objects in total). The second reason is that the trends of the different clouds seem to be similar (except for our Taurus cloud smaple which has a low number of stars). Merging the sample will strengthen our conclusions thanks to the large number of class II objects.

4. Properties of crystalline silicates in the disks around young stars

One may expect that the relatively large spectral range of the IRS instrument (5−35 μm) implies that the detected short- and long-wavelength emission features could arise from physically distinct regions in the disk. Kessler-Silacci et al. (2006) and Pinte et al. (2008), among others, have shown that for a typical TTs, the 10 μm emission comes from a region about 10 times smaller than the 20 μm emitting zone. We examine in this section the correlations between the detected features. In particular, we inspect the relation between the properties of the 10 μm silicate amorphous feature (its energy, the size of its carriers, its apparition frequency) and those of the crystalline silicate features at $\lambda > 20$ μm.

4.1. Growth of warm amorphous silicates

The amorphous 10 μm feature is present at a rate of about 70% in our sample. Bouwman et al. (2001), van Boekel et al. (2003) and Kessler-Silacci et al. (2006) have shown that detailed studies of this feature reveal much information on dust characteristics. Especially noteworthy is that the observed shape versus strength relation for the 10 μm feature can be reproduced by varying the characteristic grain size over the range of 0.1−3 μm. Here we analyse the 10 μm feature by adopting the same continuum normalization and the same computational method for the shape (flux ratio $S_{11.3}/S_{9.8}$) and strength ($S_{\rm Peak}^{10\,\mu{\rm m}}$) of the 10 μm feature as in Kessler-Silacci et al. (2006). The different values $S_{11.3}$, $S_{9.8}$ and $S_{\rm Peak}$ are obtained by normalizing the observed flux F_ν as follows: $S_\nu = 1 + (F_\nu - F_{\nu,{\rm c}})/\langle F_{\nu,{\rm c}}\rangle$, where $F_{\nu,{\rm c}}$ is the estimated linear continuum between the red and blue feet of the feature and $\langle F_{\nu,{\rm c}}\rangle$ its mean value between the two feet (all fluxes expressed in Jy). We choose a wavelength range of ±0.1 μm around 9.8 μm and 11.3 μm to calculate $S_{11.3}$ and $S_{9.8}$.

Figure 5 (left panel) shows the known correlation between the flux ratio $S_{11.3}/S_{9.8}$ (10 μm feature shape) and $S_{\rm Peak}$ (10 μm feature strength). To quantify this correlation we use a Kendall τ test. The Kendall τ rank correlation coefficient measures the degree of correspondance between two datasets. If the agreement between the two sets of values is perfect then $\tau = 1$, if the disagreement is perfect then $\tau = -1$. The Kendall τ procedure also returns a probability P, computed using the complementary error function of $|\tau|$ (see Press et al. 1992, for further informations on the Kendall τ and P calculations). The P probability is the two-sided significance; the smaller the P value, the more significant the correlation.

For the shape versus strength of the amorphous 10 μm feature, we find an anti-correlation ($\tau = -0.42$) with a significance probability $P = 3.58 \times 10^{-7}$. This correlation can be interpreted as larger grains producing a flatter 10 μm amorphous feature, while smaller grains produce narrower features (e.g. van Boekel et al. 2003). A thorough analysis by Kessler-Silacci et al. (2006) and Kessler-Silacci et al. (2007) of the shape-strength trend showed that more massive stars (HAeBe) tend to have sharper 10 μm features than do TTs and BDs, which cluster in a region more consistent with micron-diameter grains as the typical emitting grain size. The comparison of our observations to synthetic 10 μm amorphous features calculated for different grain sizes (see Sect. 4.6 for details on the computation method of grain opacities) confirms this trend as the bulk of our sample clusters in a region consistent with grains that have grown to sizes larger than about 2 μm (left panel of Fig. 5).

4.2. Growth of cold crystalline silicates

Although a similar analysis of the 20 μm amorphous emission features is rendered more difficult because of the broadness of the feature, the narrower longer-wavelength crystalline silicate features, especially the C23 complex, show a grain size-dependent behaviour that can be tested with our disk sample (see the theoretical opacities in Fig. 9). Similar trends could not be exploited for the C28 complex as its shape is not very sensitive to grain size (over the 0.1−3 μm range). For the C23 complex, we build a feature shape index, the S_{24}/S_{23} flux ratio, computed

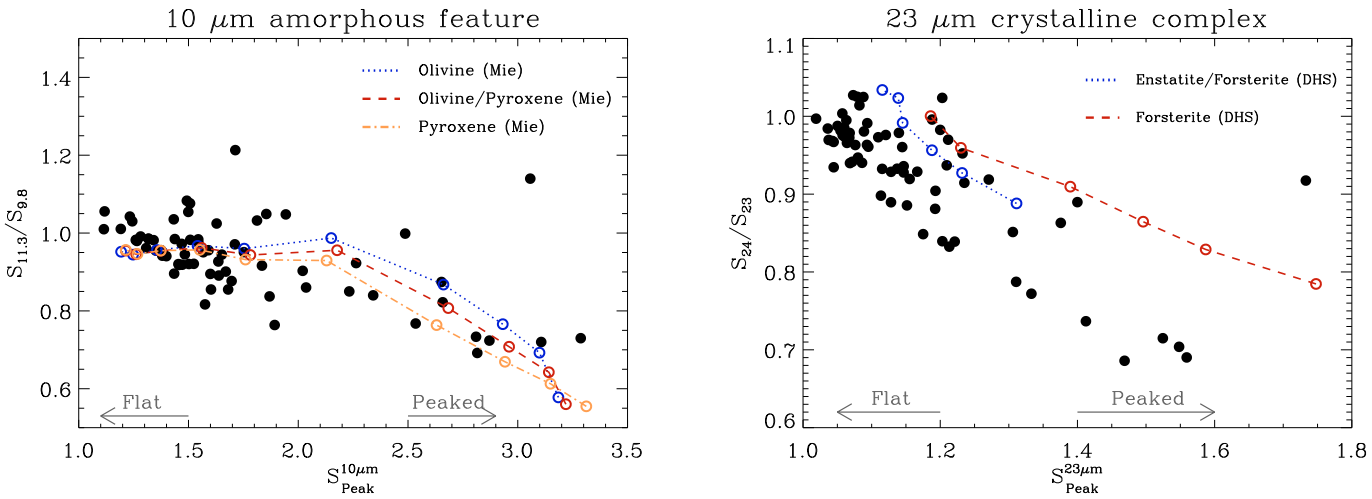

Fig. 5. *Left panel*: correlations between shape ($S_{11.3}/S_{9.8}$) and strength ($S_{\rm Peak}$) of the amorphous 10 μm feature. *Right panel*: shape (S_{24}/S_{23}) versus strength ($S_{\rm Peak}$) for the C23 μm crystalline complex. Colored points and curves are derived from theoretical opacities for different mixtures. For every curve on *left panel*, the open circles represent different grain sizes, *from bottom to top*, 0.1, 1.0, 1.25, 1.5, 2.0, 2.7, 3.25, 4.3, 5.2, and 6.25 μm. For every curve on *right panel*, the grain sizes are, *from bottom to top*, 0.1, 1.0, 1.25, 1.5, 2.0 and 2.7 μm.

using the same approach as for the amorphous 10 μm feature. The S_{23} normalized flux is obtained by averaging the normalized (local) continuum-subtracted flux between 23.5 and 23.8 μm, and between 24.1 and 24.4 μm for S_{24}. Figure 5 (right panel) shows the S_{24}/S_{23} ratio as a function of the strength of the C23 complex (C23 $S_{\rm Peak}$). The Kendall test gives $\tau = -0.54$ with a significance probability below 10^{-38}, indicative of a clear anticorrelation between these two quantities.

To better evaluate the relationship between grain size and the C23 shape, we calculate theoretical S_{24}/S_{23} ratios for synthetic crystalline silicates opacity curves obtained using the Distribution of Hollow Spheres (DHS) method (Min et al. 2005). We consider grains between 0.1 and 2.7 μm in radius, and two different compositions: 100% forsterite (Mg_2SiO_4, using optical constants from Servoin & Piriou 1973) and a mixture composed of 50% forsterite plus 50% enstatite ($MgSiO_3$, optical constants taken from Jaeger et al. 1998). Grains larger than ~3.0 μm, for either enstatite or forsterite, do not give striking results, as the feature disappears into the continuum. Also, a pure enstatite composition turns out to be incompatible with the observed shape for the C23 complex as it shows two unblended features at 23.8 and 24.5 μm. This indicates that we are not observing pure enstatite grains in our sample, a result which seems to first order consistent with Bouwman et al. (2008) who found that the very inner (~1 AU) warm dust population is dominated by enstatite while the dust population at large radii is dominated by forsterite. The overall shape-strength trend for the C23 crystalline complex is better reproduced for a forsterite/enstatite mixture, with characteristic grain sizes larger than 1.0 μm in order to match the bulk of the measured values. This suggests that not only have the warm amorphous silicate grains grown in our sample of TTs (left panel of Fig. 5), but also that the colder crystalline silicate grains have coagulated into μm-sized particles and remain suspended in the upper layers of the disk atmospheres.

The offset in the right panel of Fig. 5 between the data points distribution and the curves obtained using theoretical opacities may come from various effects. First, we consider pure crystalline dust grains, which may be a too restrictive assumption to reproduce the observations. It allows us to see the impact of grain size, however, and to show that it matches reasonably well with the observed trend. Recently, Min et al. (2008) studied the impact of inclusions of small crystals into larger amorphous grains, but this is too much of a refinement for our purposes. Second, we only consider pure Mg-rich crystals (no iron). According to Chihara et al. (2002), the 24.5 μm feature of crystalline pyroxenes shifts towards slightly larger wavelengths with increasing Fe-content. Also, according to Koike et al. (2003), the peak position of the 23.8 μm crystalline olivine feature does not shift unless the Fe-content is larger than 20%. As the S_{24} index is computed integrating between 24.1 and 24.4 μm, raising the Fe-content will produce a smaller S_{24} and therefore a smaller S_{24}/S_{23}, while the strength of the complex will decrease slightly as the 24.5 μm feature shifts to larger wavelengths. To conclude, even if there is a small shift when comparing the observations to theoretical points, the trend is well reproduced by varying the grain size.

Interestingly, we find no correlation between the grain size proxy for the amorphous 10 μm feature and the grain size proxy for the C23 complex. Considering the sets of values $(S_{11.3}/S_{9.8})/S^{10}_{\rm Peak}$ as a function of $(S_{24}/S_{23})/S^{23}_{\rm Peak}$, we obtain a Kendall's τ of 0.07, with a significance probability P of 0.44. This means that even if grain growth took place in both components, the growth of the amorphous and crystalline grains, respectively, does not seem to be correlated.

4.3. Relationship between the 10 μm and C23 features with disk properties

Young flared disks are expected to show rising spectra in the mid-IR, as opposed to more evolved, settled systems having self-shadowed disks with much flatter mid-IR spectra (e.g. Dominik et al. 2003). Here we measure the slope of the spectra by the ratio of the F_{30} and F_{13} indexes, where F_{13} is the mean flux value (in Jy) in the range 13 μm ± 0.5 μm, and between 29 μm and 31 μm for F_{30}. The left panel of Fig. 6 shows the correlation between the strength of the amorphous 10 μm feature and the slope of the spectra (F_{30}/F_{13} ratio). Taking out the two outliers (blue open circles), which are known cold disks (LkHα 330 and CoKu Tau/4, Brown et al. 2007), we find a correlation coefficient $\tau = 0.29$ with a significance probability P smaller than

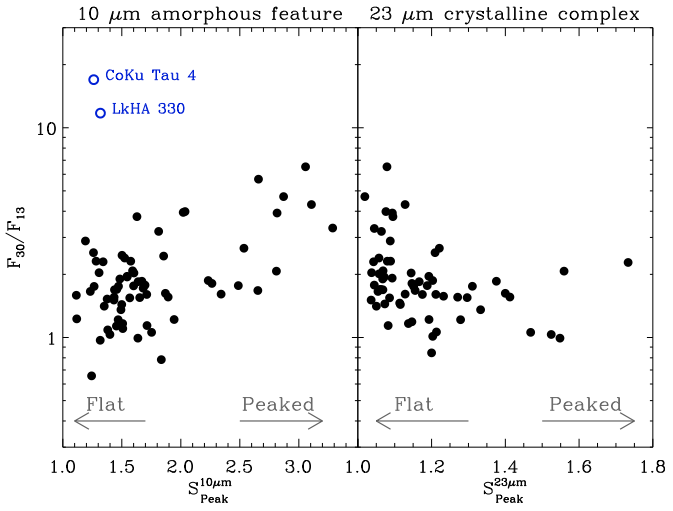

Fig. 6. *Left panel*: correlations between the slope of spectra (F_{30}/F_{13}) as a function of the strength ($S_{\rm Peak}$) of the amorphous 10 μm feature. The two outliers (blue open circles) are cold disks: LkHα 330 and CoKu Tau/4. *Right panel*: spectral slope (F_{30}/F_{13}) versus strength ($S_{\rm Peak}$) for the C23 μm crystalline complex.

5.2×10^{-4} suggestive of a correlation. A similar trend is found by Bouwman et al. (2008) within their FEPS sample of seven stars, and by Watson et al. (2009) with the Taurus-Auriga sample of 84 TTs. This can be interpreted as smaller grains (large $S^{10\,\mu{\rm m}}_{\rm Peak}$ values) being probed in flared disks (high values of F_{30}/F_{13}), while flattened disk (low F_{30}/F_{13} values) atmospheres are characterized by larger grains.

If dust sedimentation is the main process responsible for disk flattening, one would expect the upper layers of the disks to be depleted in large grains, hence the mid-infrared spectroscopic signature to be that of very small grains (peaked 10 μm features). The observed trend (Fig. 6) very clearly refutes such a possible trend in the relation between the SED shape and that of the 10 μm feature. The effect of dust sedimentation on the shape of the 10 μm amorphous silicate feature was recently discussed by Dullemond & Dominik (2008) based on models. They showed that the sedimentation of the larger grains toward the disk midplane is generally not enough to transform a flat 10 μm feature into a peaked feature. Our observations tend to support these results as sedimentation, if assumed to be revealed by disk flattening, is generally associated with flat 10 μm features. This trend is in fact valid for the majority of the TTs in our sample as the objects cluster in the region with flat SEDs and flat silicate features in Fig. 6.

For the C23 crystalline complex (right panel of Fig. 6), we find a rather weak anticorrelation, with $\tau = -0.21$ and a significance probability $P < 0.01$. The small crystalline grains with $S_{\rm Peak}$ larger than about 1.2 are only found in flat or slowly rising disks (F_{30}/F_{13} smaller than about 2), while the larger grains can be found in all kinds of disks. Interestingly, the very flared disks which have large crystalline grains emitting at 23 μm also show small amorphous grains in their warm component (that is, the region probed at 10 μm). Seven out of the eight objects (RY Lup, RX J1615.3-3255, Haro 1-1, SSTc2d J162148.5-234027, SSTc2d J162245.4-243124, SSTc2d J162715.1-245139, Haro 1-16) with $F_{30}/F_{13} > 3$ on the right panel of Fig. 6 indeed have their counterpart in the left panel with $S^{10}_{\rm Peak}$ larger than about 2 (the last object being DoAr 25).

4.4. Relationship between the 10 μm feature and crystallinity

We find in Sect. 4.2 that the growth of warm amorphous silicates (probed by the 10 μm feature) is statistically disconnected from the growth of cold crystalline silicates (probed by the C23 complex). We further investigate the relationship between the amorphous and crystalline silicates features by searching for a correlation between the energy contained in the amorphous 10 μm feature and the energy contained in the C23, C28 and the 33.6 μm features. To get rid of possible distance or brightness effects we normalized the line fluxes as follows: Line flux [unitless] = Line flux[W m^{-2}]/($\lambda\langle F_{\lambda,{\rm c}}\rangle$), where $\langle F_{\lambda,{\rm c}}\rangle$ is the mean value of the local feature continuum and λ is the measured central wavelength of the considered feature.

The unitless line fluxes are displayed in the left panel of Fig. 7, which shows that when both the C23 and the 10 μm feature are present with $SNR > 20$, their emission energies are not correlated ($\tau = 0.06$, significance probability $P = 0.55$), although the plot would suggest that objects with low 10 μm line flux usually also have a low C23 line flux. The middle panel of Fig. 7 shows a similar result when both the C28 and the 10 μm feature are present with $SNR > 20$: $\tau = 0.023$ (no correlation between these features) with a significance probability $P = 0.83$, reflecting the dispersion. Finally, the right panel of Fig. 7 shows a similar trend for the 33.6 μm and the amorphous 10 μm feature: $\tau = 0.22$ and a significance probability $P = 0.15$. Therefore, the flux radiated by the 10 μm amorphous feature is largely unrelated to the energy contained in the crystalline silicates features that appear at wavelengths longer than 20 μm.

Similarly, the shape of the amorphous 10 μm feature (that is, the $S_{11.3}/S_{9.8}$ ratio, which is a proxy for grain size, Sect. 4.1) seems uncorrelated with the emergence of the 23 μm complex, the 28 μm complex, or the 33.6 μm forsterite feature. The right panel of Fig. 7, for example, shows the number of positive detections of the C23, C28 and 33.6 μm features per $S_{11.3}/S_{9.8}$ bin, where the errors bars correspond to Poisson noise (square root of the number of detections). The fraction of disks with C23 and C28 features is found to be independent of the mean grain size probed by the 10 μm amorphous feature, further suggesting that the 10 μm feature and the C23, C28 features essentially probe disconnected populations. For the 33.6 μm feature, the fraction of objects per bin seems less independent because of the smaller numbers of detections (23 objects with both the 10 and 33.6 μm features).

Overall, these results suggest that the crystalline features appearing at wavelengths longer than 20 μm and the 10 μm amorphous feature arise from unrelated populations. On the other hand, Fig. 8 shows the correlation between the normalized line fluxes of the C23 and C28 complexes where both are present with $SNR > 20$, and also their correlation with the 33.6 μm feature. The Kendall τ tests and associated significance probabilities confirm the expected result that the crystalline features at wavelengths longer than 20 μm have emission fluxes that correlate to each other.

4.5. Feature correlation coefficients

The one-to-one correlation probabilities between the detection frequencies of all the features examined in this study with $SNR > 20$ are displayed in Table 3. The diagonal shows the total number of positive detections for any given feature (these numbers being close to percentages of detections as we have 96 objects). The lower part of the table displays the Kendall τ values as well as the number of spectra with common detections of the

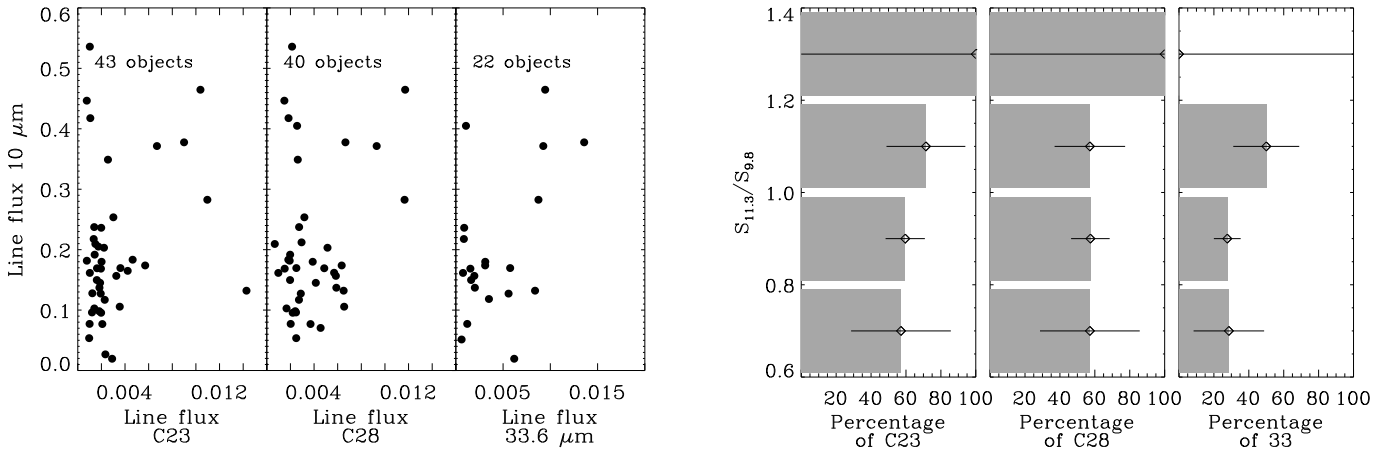

Fig. 7. *Left panel*: *from left to right*: correlations between the unitless line fluxes of the 10 μm feature and the C23, C28 complexes plus 33.6 μm forsterite feature. *Right panel*: *from left to right*: percentages of objects showing the C23/C28 complexes and 33.6 μm forsterite feature as a function of the shape of the 10 μm feature. Larger, amorphous grains are located at *the top* of the plot.

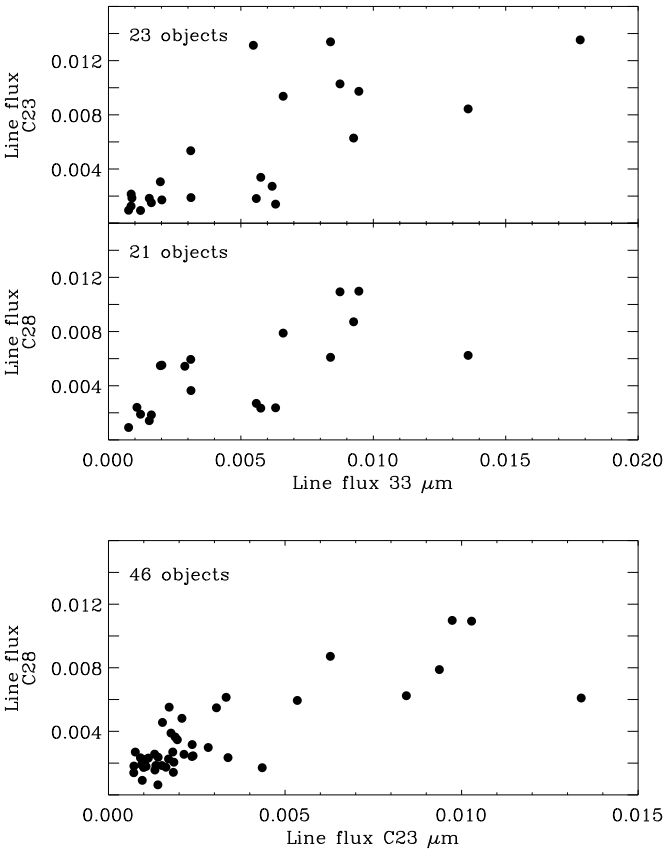

Fig. 8. *Top panel*: normalized line fluxes for the 33.6 μm feature and the C23 complex (Kendal $\tau = 0.55$ and significance probability $P = 2.41 \times 10^{-4}$). *Middle panel*: same but with the C28 complex ($\tau = 0.56$, $P = 3.66 \times 10^{-4}$). *Bottom panel*: normalized line fluxes between the C23 and C28 complexes ($\tau = 0.54$, $P = 1.19 \times 10^{-7}$).

considered features between parenthesis. The Kendall significance P probabilities are displayed in the upper part.

At this point, it is interesting to understand the meaning of the inferred Kendall τ values in this table. Some correlations appear possible according to the Kendall τ values but only because both features are absent from spectra. Consider as an example the 11.3 μm forsterite feature and the C23 complex, for which we obtain $\tau = 0.244$ and $P = 0.001$, for 12 detections of the 11.3 μm feature and 56 detections of the C23 complex, indicating a weak correlation. Out of the 96 stars, 11 spectra show both features, one spectrum shows the 11.3 μm feature only, and 45 objects show the C23 complex only. The other 39 (96 – 45 – 1 – 11) objects show neither the 11.3 μm feature nor the C23 complex, and these objects account for concordant pairs. This explains why we find a weak correlation (non-zero τ value), as the number of concordant pairs (50) is of the order of the number of discordant pairs (46) for this example. In this case, we could eliminate objects that do not show either of these two features from the statistics, and we would obtain an anti-correlation with $\tau = -0.25$ and $P = 0.004$. Therefore, in order to have comparable numbers for all the features, irrespective of the number of detections, we decide to consider the entire sample for the calculation of the correlation coefficients, even when spectra do not show any of the considered features.

The detection frequencies of the 10 μm amorphous feature and the C23 complex are found to be essentially uncorrelated ($\tau = 0.051$ with $P = 0.47$). Similar results are obtained when considering the 10 μm feature and the C28 complex ($\tau = 0.013$ with $P = 0.86$), and also the 10 μm and 33.6 μm features ($\tau = 0.055$ with $P = 0.44$). For the C23, C28 complexes and the 33.6 μm feature, we have, respectively, 43, 40 and 22 common detections with the amorphous 10 μm feature (which is observed in 69 spectra). The C23 and C28 complexes, as well as the 33.6 μm forsterite feature, do therefore appear in spectra independently from the presence of the 10 μm feature. On the other hand, the C23 complex appears to be coincident with the C28 complex in our spectra ($\tau = 0.619$ with $P < 10^{-38}$), which concurs with our results based on line fluxes (Sect. 4.4). The 33.6 μm feature also appears to be coincident, to a slightly lesser extent with the C23 complex ($\tau = 0.288$ with $P < 10^{-38}$), and the C28 features ($\tau = 0.233$ with $P = 3 \times 10^{-3}$). The number of common detections also confirm these trends.

Table 3 further shows that the forsterite 11.3 μm feature is anti-correlated with the amorphous 10 μm feature ($\tau = -0.44$, only 3 objects show both the 10 μm and the 11.3 μm features). The anti-correlation between the forsterite 11.3 μm feature and the amorphous 10 μm feature could be explained by a contrast effect. Indeed, the 11.3 μm feature could potentially be present

Table 3. Correlation coefficients between the features detected with *SNR* > 20.

	9.2 μm	10.0 μm	11.3 μm	12.5 μm	16.2 μm	21.6 μm	C23	25.0 μm	C28	33.6 μm
9.2 μm	**15**	0.008	0.238	0.012	0.003	0.622	0.000	0.887	0.000	0.195
10.0 μm	0.187 (14)	**69**	0.000	0.293	0.049	0.088	0.468	0.203	0.858	0.441
11.3 μm	–0.084 (1)	–0.447 (3)	**12**	0.556	0.557	0.056	0.001	0.363	0.000	0.182
12.5 μm	0.179 (4)	0.075 (10)	0.042 (2)	**12**	0.087	0.308	0.113	0.003	0.004	0.182
16.2 μm	0.211 (6)	–0.140 (12)	0.042 (3)	0.121 (4)	**19**	0.000	0.000	0.732	0.115	0.068
21.6 μm	0.035 (2)	0.121 (9)	–0.135 (1)	0.072 (2)	0.253 (5)	**10**	0.053	0.025	0.025	0.963
C23	0.354 (15)	0.051 (43)	0.244 (11)	0.112 (9)	0.299 (17)	0.137 (8)	**56**	0.000	0.000	0.000
25.0 μm	–0.010 (2)	0.090 (11)	–0.064 (1)	0.214 (4)	0.024 (3)	0.159 (3)	0.325 (13)	**13**	0.178	0.318
C28	0.260 (13)	0.013 (40)	0.332 (12)	0.202 (10)	0.112 (13)	0.158 (8)	0.619 (46)	0.095 (9)	**53**	0.001
33.6 μm	0.092 (6)	0.055 (22)	0.095 (5)	0.095 (5)	0.129 (8)	–0.003 (3)	0.288 (23)	0.071 (5)	0.233 (21)	**28**

but hidden by the stronger amorphous feature (see discussion in Sect. 4.6 for a more detailed analysis of this effect).

Interestingly, the crystalline features in the 10 μm range (9.2 and 11.3 μm) seem to be correlated with both the C23 and C28 complexes: if crystalline features are present in the 10 μm spectral range then the presence of the two complexes is highly probable. Still the reverse is not true, if one of the two complexes (C23 or C28) is present, it is not guaranteed that we will find the 9.2 or 11.3 μm features. This reflects that the correlation is dominated by objects where none of the considered features is present. Furthermore, as we find no strong correlation for the line fluxes between these features, this would mean that there is a general increase of crystallinity for several objects, compared to the rest of the sample. Also, the two features at 9.2 and 11.3 μm do not seem to be correlated with the 33.6 μm forsterite feature. The declining quality of the data (lower *SNR*) at the long wavelength end of the IRS spectra may explain this trend in part, as some (lower contrast) 33.6 μm features may not have been detected. Another possible explanation could be that the 33.6 μm forsterite feature probes an even colder disk region than the population probed by C23 and C28 complexes.

To summarize, our results show that the C23, C28 and 33.6 μm crystalline features probably arise from the same population of grains. Also, the detections of the 9.2 and 11.3 μm crystalline features are correlated with the detections of C23 and C28 (but the presence of one of the longer wavelengths complexes does not guarantee the detection of 9.2 or 11.3 μm features), which can be interpreted as a general increase of crystallinity in the inner and outer regions of disks. However, this crystalline population seems to be disjoint from the population of amorphous silicate grains that produce the 10 μm feature.

4.6. Degree of crystallinity of the warm versus cold disk regions

Both Figs. 3 and 4 show larger occurrences of the C23 and C28 emission features than of shorter wavelength crystalline silicate features, especially the 9.2 (enstatite) and 11.3 μm (forsterite) features. As silicates are expected to thermally anneal close to the star, this result may reflect a counterintuitive positive gradient of the crystalline silicate fraction toward colder temperatures. However, the presence of the broad, and generally strong, amorphous 10 μm feature may lower the contrast of (or even hide) the shortest wavelength crystalline features preventing direct conclusions. We examine in this section this apparent *crystallinity paradox* by comparing our Spitzer/IRS observations to synthetic spectra.

To better gauge the actual differences between the degrees of crystallinity of the warm ($\lambda \sim 10$ μm) versus cold ($\lambda > 20$ μm) disk regions, we generate synthetic spectra representative of the observations, from which we then extract line fluxes as was performed for the IRS spectra in Sect. 3.2.1. We consider amorphous species that include silicates of olivine stoichiometry (glassy $MgFeSiO_4$, optical constants from Dorschner et al. 1995), and silicates of pyroxene stoichiometry (glassy $MgFeSi_2O_6$, optical constants from Dorschner et al. 1995). For the crystalline species, we use enstatite ($MgSiO_3$) optical constants from Jaeger et al. (1998) and forsterite (Mg_2SiO_4) optical constants from Servoin & Piriou (1973). Theoretical mass opacities κ_λ are computed using Mie theory (valid for hard spheres) for the amorphous species and DHS theory (Distribution of Hollow Spheres, Min et al. 2005) for the crystalline silicates. Twelve example opacity curves for the four compositions and three typical (in terms of spectroscopic signature) grain sizes (0.1 μm, 1.5 μm and 6.0 μm) are displayed in Fig. 9.

The synthetic spectra of Fig. 10 have been generated by adding to a representative continuum (C_ν), the mass opacities of amorphous and crystalline silicates, multiplied by relative masses and by a blackbody at reference temperatures (350 K for the warm region, and 100 K for cold region). The amorphous content is a 50:50 mixture of olivine and pyroxene and the crystalline content is a 50:50 mixture of enstatite plus forsterite. The adopted 10 μm representative continuum is given by the median values (mean slopes and mean offsets: $C_\nu = \bar{a} \times \lambda + \bar{b}$) of all the local continua linearly ($C_\nu^i = a^i \times \lambda + b^i$) estimated in Sect. 3.2.1 for the observed amorphous 10 μm features: $C_\nu = 0.01 \times \lambda + 0.097$, with C_ν in Jy and λ in μm. Similarly, a representative C23/C28 continuum has been derived for cold synthetic spectra: $C_\nu = -0.001 \times \lambda + 0.43$ (C_ν in Jy and λ in μm).

To obtain as representative synthetic spectra as possible, we compute the median observed continuum over feature ratio (i.e., the continuum flux divided by the height of the feature) for the 10 μm feature and the C23 complex. For the amorphous 10 μm feature, we obtain a ratio of 2 and we therefore normalize the opacities, before adding them to the continuum (C_ν), so that the synthetic spectra show similar ratios. For the C23, we measure a median continuum over feature ratio of 20 ± 10, and we normalize the opacities in order to get a ratio between 10 and 30 in the synthetic spectra. This exercise could not be reproduced for the large 6.0 μm grains because the shapes of their C23/C28 features are not representative of the observed features (especially for the forsterite grains, see right panel of Fig. 9), suggesting such large grains are not the main carriers of these features. As a final step, the synthetic spectra are degraded by adding random noise, with a maximum amplitude of 1.8×10^{-3} Jy for the warm spectra and 7.2×10^{-3} for the cold spectra, representative of the quadratic sum of the measured uncertainties on the Spitzer data over in the 10 μm region and in the C23/C28 spectral range. The

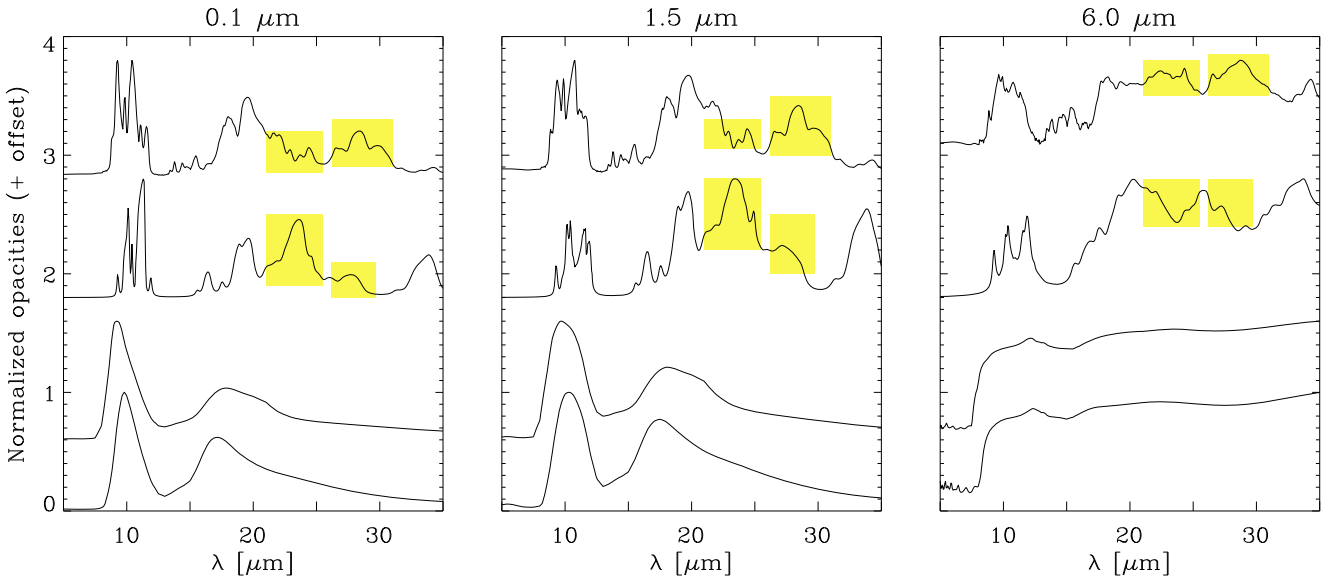

Fig. 9. Example mass opacities (in arbitrary units) used to model the IRS observations. *From bottom to top*: amorphous olivine, amorphous pyroxene, crystalline forsterite and crystalline enstatite. *The left panel* shows opacities for a grain size $a = 0.1$ μm, $a = 1.5$ μm for *the middle panel* and $a = 6.0$ μm for *the right panel*. Some of the features discussed in Sects. 3.1.1 and 3.1.3 can be recognized. Yellow boxes are places of both C23 and C28 crystalline complexes.

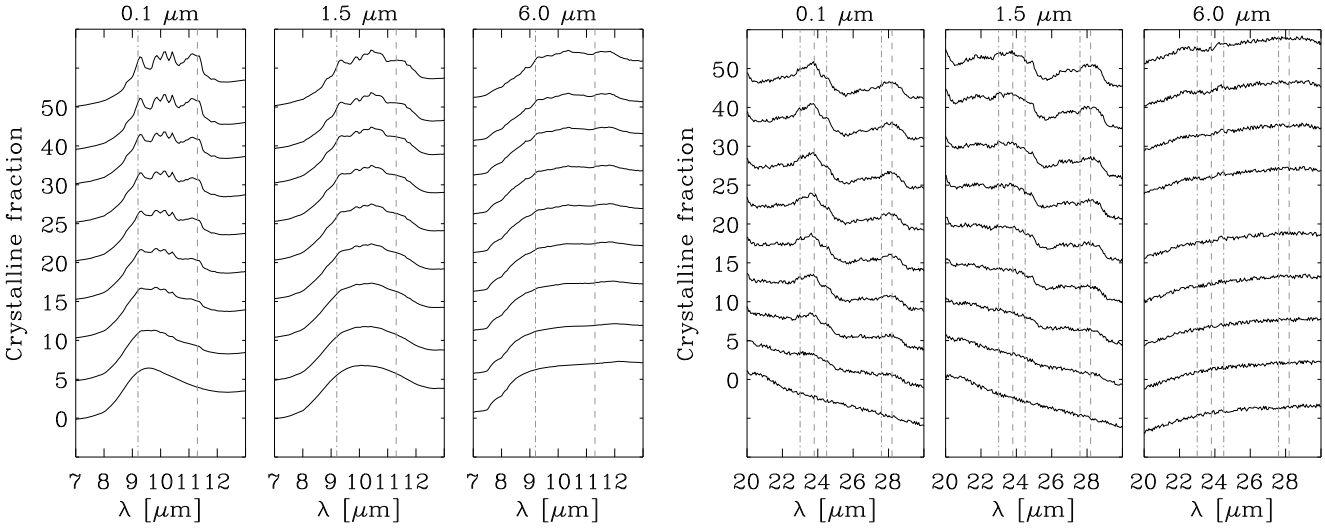

Fig. 10. Synthetic spectra, in arbitrary units, for mass fractions of crystalline silicates from 0% to 50% (steps are: 0, 5, 10, 15, 20, 25, 30, 40, 50%, see Sect. 4.6 for more details). The impact of the grain size on the detectability of the 11.3 μm, C23 and C28 features is considered for 0.1 μm, 1.5 μm and 6.0 μm grains.

synthetic observations displayed in Fig. 10 are then processed as in Sect. 3.2.1 to derive the band fluxes of the crystalline features.

The theoretical *SNR*s for the 9.2, 11.3 μm, C23 and C28 crystalline silicate features, assuming crystalline mass fractions between 0% and 50% and characteristic grain sizes, are displayed in Fig. 11. It is seen that the *SNR* reached in the simulations compare well with the measured *SNR* values, especially for micron-sized grains (Table 5). The diagonal-striped areas correspond to crystalline mass fractions where the continuum over C23/C28 feature ratios could hardly match the median observed values, or which totally fail to reproduce them. This means that we are not able to discuss the detectability of features for crystalline mass fractions smaller than 5 and 15% for grains sizes of 0.1 and 1.5 μm, respectively. In the particular case of the 6.0 μm grains, as explained above, we cannot compute *SNR* for C23 and C28 complexes as opacities do not match typical observations.

We see in Fig. 11 that the *SNR* of the crystalline features drops with increasing grain size (especially the 9.2 μm, 11.3 μm features) and with decreasing crystalline mass fraction, as expected. A crystalline fraction of ~5% or larger seems to be enough that all four of the studied crystalline features are observable if the grains are sub-micron in size. For the 1.5 μm-sized grains, crystalline mass fractions of about 15% are required, (1) to obtain spectra consistent with observations; and (2) to detect all the features studied with *SNR* > 20. For higher

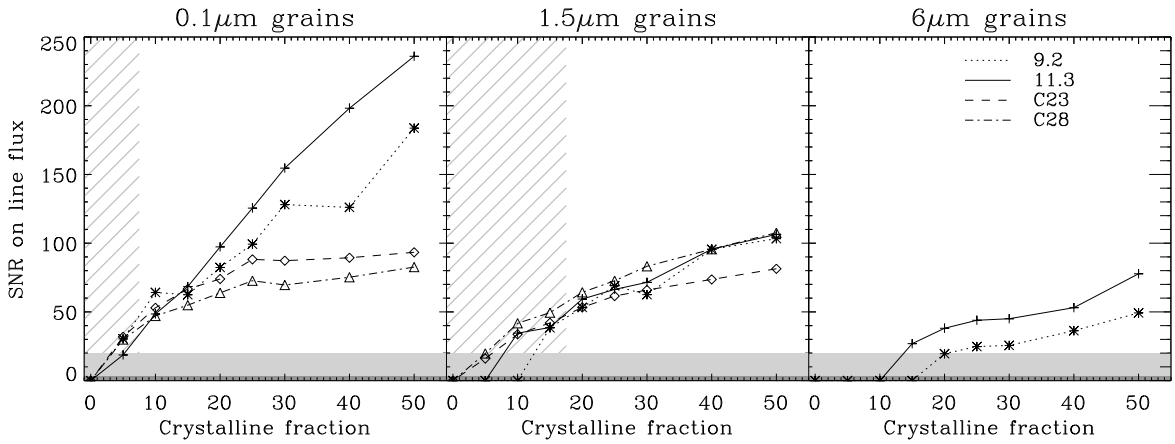

Fig. 11. Signal-to-noise ratio of the 9.2 μm, 11.3 μm, C23 and C28 integrated line fluxes measured as in Sect. 3.2.1 but on the synthetic spectra displayed in Fig. 10 (see text for details about the models). The light gray area represents the conservative detection threshold used in this paper ($SNR = 20$), while the dark gray area shows the $SNR = 3$ limit. Grey diagonal stripes are the loci where theoretical opacities are not consistent with typical observations.

crystalline mass fractions, they all present very similar behaviors. For 6.0 μm-sized grains, it becomes more difficult to trace the detectability of the C23 and C28 features as opacities become much less consistent with typical observations. For 9.2 μm and 11.3 μm, crystalline fractions larger than 20% and 15%, respectively, are required in order to detect these features with $SNR > 20$.

Since the observed features in our sample are mainly produced by μm-sized grains (Sect. 4.1), which in particular produce a shoulder at the location of the 11.3 μm crystalline feature, we conclude that the physical processes that preferentially place μm-sized grains in the disk atmospheres do not contribute much to the measured differences between the number of detections of the 11.3 μm feature compared to the number of detections of the C23 complex (Figs. 3 and 4).

To summarize, we find an apparent *crystallinity paradox*, namely a noticeable difference in detection statistics for the 11.3 μm and C23 features, with more than 3 times more detections for C23 compared to the number of detections of the 11.3 μm forsterite feature. This seems counterintuitive as shorter wavelengths are expected to probe warmer disk regions where grains can crystallize more efficiently. We investigated the possibility that crystalline features could be hidden by amorphous features. The effect seems insufficient to explain the observations, but we cannot predict firmly the real impact of this effect until the Spitzer observations are confronted by a more detailed compositional analysis. This is deferred to a future paper (Olofsson et al. 2009b, in prep.).

5. Discussion

5.1. On the lack of Fe-rich silicates

Because of the large number of objects analysed in this paper, our results raise challenging questions on the dynamics and (chemical) evolution of planet-forming disks regions that are in principle not statistically biased. For instance, the lack of Fe-rich silicates in our 96 star sample[2] reinforces the result by Bouwman et al. (2008) obtained with their 7-star sample. Silicates crystals studied in this analysis may contain iron, as seen in Sect. 3.1.2 but magnesium is the most abundant element. Several scenarios can explain this apparent lack of iron. First, Davoisne et al. (2006) found that a reduction reaction during the thermal annealing of ferro-magnesian amorphous silicates at temperatures below 1000 K can produce pure forsterite crystals plus spheroidal metallic particles. The iron is therefore locked inside a metallic nanophase that cannot be observed. Secondly, according to Nuth & Johnson (2006), simple thermal annealing in the warm inner regions of the disk cannot produce Fe-rich silicate crystals. As the annealing timescale for iron silicates is larger than for magnesium silicates (Hallenbeck et al. 2000), the lifetime of such Fe-rich silicates against the evaporation timescale is expected to be too short for these grains to crystallize and then be transported outward in the disk. Still, thermal annealing induced by shocks may be able to produce both Fe-rich and Mg-rich crystals at the same time.

[2] Except 5 marginal detections discussed in Sect. 3.1.2.

5.2. On the need for turbulent diffusion and grain-grain fragmentation

The new grain size proxy introduced here for cold crystalline silicates (via the C23 complex) indicates that the upper layers of the disks are preferentially populated by μm-sized grains. This result also holds for the warm disk region using the classical size proxy for the carriers of the 10 μm amorphous feature (Fig. 5). Adopting a purely sequential evolutionary approach for the solid constituents in disks, where interstellar-like grains coagulate to form micron-sized dust aggregates, then pebbles and planetesimals, a straighforward conclusion from these results would be that grain agglomeration occurred in the first few AU and that we are witnessing an intermediate, regular step of the growth of solid particles along their way to form planets. Nevertheless, this picture is most certainly an oversimplified view of the processes at work in planet-forming regions around young stars as it does not fit with basic dynamical considerations. Indeed, the short settling time-scale of μm-sized grains in a laminar disk, and their expected fast growth which will accelerate sedimentation (Dullemond & Dominik 2005; Laibe et al. 2008), both argue in favor of some processes that sustain the disk atmosphere with grains that have mid-infared spectroscopic signatures (grains smaller than about 10 μm) over a few Myr. Therefore, our results support the replenishment of the disk upper regions by the vertical transport of dust particles (e.g. turbulent diffusion, Fromang & Nelson 2009), likely combined with grain-grain fragmentation to balance the expected efficient growth of solid particulates

(that accelerates sedimentation, Dullemond & Dominik 2005; Laibe et al. 2008). In this picture, the grains observed at mid-IR wavelengths would then result from the destruction of much larger solid particles (an assumption consistent with the presence of millimeter-sized grains in most TTauri disks, e.g. review by Natta et al. 2007), rather than from the direct growth from interstellar-like grains.

5.3. On the depletion of submicron-sized grains

A consequence of the above conclusion is that one would have to explain the general apparent depletion of submicron-sized grains in the disk zones probed by mid-IR spectroscopy. The fact that we see a flat, boxy 10 μm feature profile for most TTs indicates that there cannot be many submicron-sized grains, because their emission would overwhelm the few large grains. Grain-grain collisions are nevertheless expected to produce fragments with a range of sizes that are likely to extend to the submicron domain (i.e. the size of the monomers that form μm-sized aggregates). This effect might be enhanced by the large velocity fluctuations (a fraction of the local sound speed) found at high altitudes above the disk midplane in disk simulations with MHD turbulence (Fromang & Nelson 2009). Qualitatively, submicron-sized grains, lifted in the disk atmospheres by turbulent diffusion or produced locally, are therefore expected to be abundant, which contradicts the IRS observations.

5.3.1. Impact of the size distribution

The above conclusion is based on our single, characteristic grain size approach (Sects. 4.1 and 4.2) and one may question whether this assumption affects our interpretation of the observations. To answer that question, we calculate mean cross-sections as follows:

$$\sigma_{\rm abs} = \int_{a_{\rm min}}^{a_{\rm max}} \pi a^2 Q_{\rm abs}(a)\, {\rm d}n(a) / \int_{a_{\rm min}}^{a_{\rm max}} {\rm d}n(a),$$

where a is the grain radius, $Q_{\rm abs}$ is the dimensionless Mie emission/absorption coefficient for a 50:50 mixture of amorphous pyroxene and olivine, and ${\rm d}n(a) \propto a^p {\rm d}a$ is the differential grain size distribution. We arbitrarily choose $a_{\rm max} = 100\,\mu$m (large enough that it does not affect the calculations for MRN-like size distributions), and we vary the minimum grain size $a_{\rm min}$ between 0.1 and 4.0 μm. Using a classical MRN ($p = -3.5$) grain size distribution, we find that the diversity of $S_{11.3}/S_{9.8}$ and $S_{\rm Peak}^{10\,\mu{\rm m}}$ values is well reproduced by adjusting the minimum grain size $a_{\rm min}$, and that the bulk of the observations is reproduced for $a_{\rm min}$ larger than 2 μm (Fig. 12), a result consistent with our single grain size analysis. Nevertheless, another way to avoid having peaked 10 μm amorphous features typical of pristine grains is to use a flatter slope for the size distribution. For example, p values larger than -3 reduce the contribution of submicron-sized grains to the mean absorption cross-section (see Fig. 12 with $p = -3$), creating an amorphous 10 μm feature that is large and boxy despite the presence of some submicron-sized grains. Therefore, the majority of the points is located at the left side of Fig. 12, which either probes μm-sized grains as the small end of the size distribution, or much flatter grain size distributions compared to the MRN, meaning that the amount of small grains is at least severely diminished in the regions probed by the Spitzer/IRS.

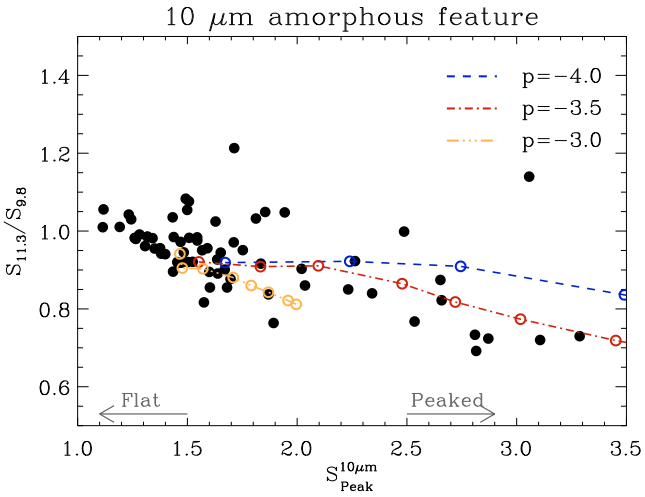

Fig. 12. Correlation between shape and strength for the amorphous 10 μm feature compared to models assuming a power law grain size distributions with indexes between -4 and -3. For each colored curve, from right to left, open circles correspond to mimimum grain sizes $a_{\rm min}$ equal to 0.1, 0.5, 0.75, 1.0, 1.5, 2.0 and 4.0 μm. For blue points only the last four mininum grain sizes are represented, for red points the 0.1 μm point is not shown, as their $S_{\rm Peak}^{10\,\mu{\rm m}}$ is larger than 3.5.

5.3.2. Impact of the crystallinity

Several studies (e.g. Bouwman et al. 2001; Honda et al. 2006; or van Boekel et al. 2005) mention the possible impact of the crystallinity on the shape versus strength correlation for the 10 μm feature. According to these studies, the presence of crystalline grains can mimic the flattening of the feature. Min et al. (2008) recently investigated in detail this effect by considering inhomogeneous aggregates. Their Fig. 2 shows that $S_{\rm Peak}^{10\,\mu{\rm m}}$ remains approximately constant for crystalline fractions up to 20% (the maximum fraction considered in their study) while $S_{11.3}/S_{9.8}$ rises, suggesting a shift along the y-axis of Fig. 12 due to crystallinity rather than along the observed trend.

In order to further investigate the impact of crystallinity on this correlation, we use the synthetic spectra described in Sect. 4.6. The only difference is that we do not normalize opacities anymore to obtain a constant ratio between feature strength and continuum. Normalizing opacities would lead to a constant $S_{\rm Peak}^{10\,\mu{\rm m}}$, which is not what we want to characterize here. We therefore normalize the opacities, for each grain size, so that only the strongest feature reaches a ratio of 2 between the continuum and the feature strength. Other features are normalized with the same factor and obviously present a higher ratio between continuum and feature strength. This normalization is done in order to reproduce spectra similar to observations, and still conserve the diversity of feature strengths. Subsequently, values for $S_{9.8}$, $S_{11.3}$ and $S_{\rm Peak}^{10\,\mu{\rm m}}$ are derived in the same way as in Sect. 4.1. Figure 13 shows the impact of crystallinity on the shape versus strength for the 10 μm feature. We consider three grain sizes (0.1, 1.5 and 6.0 μm) and the same composition as in Sect. 4.6: 50:50 mixture of olivine and pyroxene for the amorphous content and 50:50 of enstatite and forsterite for the crystalline population. The crystallinity fraction varies from 0% to 50% (0, 5, 10, 15, 20, 25, 30, 40 and 50%), and increasing crystallinity goes from bottom left to top right on the plot. We note that for 6.0 μm-sized grains the effect is negligible, while it is more dramatic for 0.1 μm-sized grains. The spread induced by an increase of crystallinity is almost orthogonal to the direction

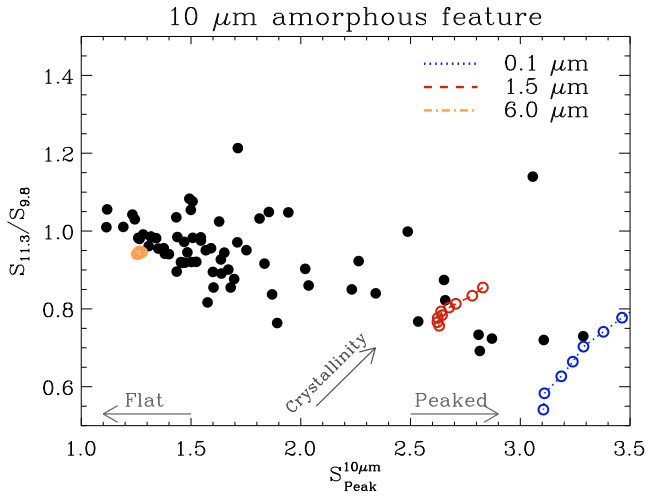

Fig. 13. Correlation between shape and strength for the amorphous 10 μm feature compared to models assuming a variation in crystallinity fraction, for three different grain sizes. For each grain size, increasing crystallinity goes from bottom left to top right, from 0% to 50% crystallinity (0, 5, 10, 15, 20, 25, 30, 40, 50%).

of the correlation. This result was also found by Kessler-Silacci et al. (2006) (Fig. 10e). The direction of this deviation can be understood when considering opacities for amorphous and crystalline grains. For the same mass of dust, crystalline grain emission will be stronger compared to amorphous grains. Therefore adding some crystalline grains to a purely amorphous dust content will give a 10 μm feature stronger *and* broader (because of crystalline features at, e.g., 11.3 μm in the case of forsterite). This will thus produce a higher value of $S_{11.3}/S_{9.8}$ and at the same time a stronger $S^{10\,\mu m}_{Peak}$.

Crystallinity therefore does impact the correlation and may be responsible for a dispersion in the direction orthogonal to the correlation, but according to the opacities, it cannot solely explain the observed trend.

5.3.3. Hypothesis for the depletion of submicron-sized grains

Several solutions could be envisaged to explain the apparent depletion of submicron-sized grains at high altitudes above the disk midplane. The fragmentation time-scale of grains in disk atmospheres may be longer than the grain growth timescale, thereby quickly eliminating the smallest and most freshly produced submicronic grains. The high velocity fluctuations observed in MHD simulations at high altitudes, do not, in principle, work in favor of this scenario. An alternative possibility may be that the submicron-sized grains are evacuated from the upper layers of the disks by stellar winds or radiation pressure. The impact of radiation pressure on grains in young disks has been explored by Takeuchi & Lin (2003) and presents several advantages. First, it acts on short timescales as long as the grain size reaches a threshold, usually referred to as the blowout size limit, below which the radiation pressure force overcomes the gravitational and gas drag forces. Second, the blowout size limit falls in the right regime of grain sizes (close to a micrometer for silicates) for solar-type stars in the presence of some gas.

It is interesting to apply the latter scenario to the case of more luminous stars. According to Kessler-Silacci et al. (2007), HAeBe stars tend to show a widest variety of 10 μm silicate features, including the peaked features attributed to submicron-sized grains. Because of their higher temperature and luminosity, HAeBe stars are expected to have upper layers that are even more ionized than those of T Tauri stars, thereby enhancing the turbulence if it is supported by disk magnetic fields, as well as velocity fluctuations. This would therefore encourage the systematic production of submicron dust fragments in disk atmospheres. On the other hand, silicate grains of a few micrometers and smaller, are in principle more prone to be eliminated by radiation pressure. Nevertheless, the latter reasoning assumes an optically thin medium at the wavelengths where grains absorb most, namely in the UV and visible. The optically thin region at mid-IR wavelengths is likely to be essentially opaque in the UV/visible, and this opacity will affect more strongly the most luminous stars, thereby possibly reducing the blowout size limit.

Clearly, the depletion of submicron-sized grains in the disk atmospheres of most T Tauri stars should be further investigated by models to examine the likelihood of the scenarios discussed above (competition between coagulation and fragmentation, stellar winds, radiation pressure, ...).

5.4. On radial mixing

The coldest disk component probed by our IRS observations shows a rather high crystallinity fraction. According to Fig. 3, the 23 and 28 μm complexes are detected in more than 50% of the spectra. In a scenario where silicate crystals form by thermal annealing, the production of crystalline silicates can only occur on reasonably short time-scales near the star ($T > 900$ K), namely in regions much hotter than those emitting at $\lambda > 20$ μm. The observed cold crystals would thus have been radially transported there from the inner disk zone, which according to two-dimensional models can occur around the midplane of accretion disks (Ciesla 2009, and references therein). Keller & Gail (2004), for example, find that ~5 to 30% of the total mass that is transported inward at high disk altitudes is transported outward near the disk midplane. For a solar mass star with an accretion rate of $\dot{M} = 10^{-6}$ $M_{\odot}$/yr, Ciesla (2009) estimates the crystalline fraction at 10 AU to be about ~40% by the end of his simulations. As the accretion rate becomes smaller, the crystalline fraction drops accordingly: ~10% and ~1% for $\dot{M} = 10^{-7}$ $M_{\odot}$/yr and 10^{-8} $M_{\odot}$/yr, respectively. However, Watson et al. (2009) find only a weak correlation between the accretion rate and the crystalline features arising at around 10 μm, and no correlation with the 33 μm feature, leading the authors to suggest that some mechanisms may be erasing such trends. Alternatively, other crystallisation processes at colder temperatures (e.g. via nebular shock, Desch & Connolly 2002) could also contribute to the presence of crystals at significant distances from the central object (e.g. Kimura et al. 2008).

It is noteworthy that the warmer disk zone seems significantly less crystalline than the colder regions, although detailed compositional analysis of the IRS spectra is required before firmly concluding this must be so (Olofsson et al. 2009b, in prep.) Interestingly, compositional fits to some individual IRS spectra by Bouy et al. (2008) and Sargent et al. (2009) do show the need for larger amounts of silicate crystals in the outer regions compared to inner regions (e.g. 2MASS J04442713+2512164 and F04147+2822). If radial mixing leads to the large crystalline fraction in the cold disk component, it leaves the disks with an inhomogeneous chemical composition in the solid phase. Some re-amorphisation processing of the crystalline grains, by X-ray emission or cosmics rays for example, could also contribute to the apparent lack of crystals in the inner regions of disks.

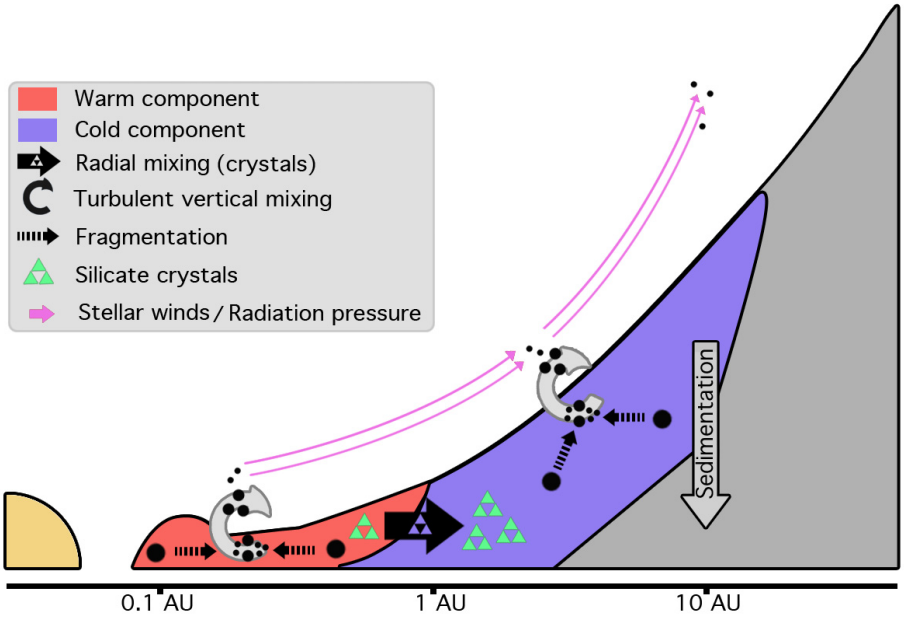

Fig. 14. Schematic view of the TTauri disk regions probed by the Spitzer IRS spectroscopic observations. This illustrates some of the dynamical processes that are discussed in Sect. 5 and summarized in Sect. 6.

This result of a cold region being more crystalline compared to the inner warm regions seems, at first glance, to be in contradiction with the results by van Boekel et al. (2004) who observed three HAeBe stars with the mid-IR instrument MIDI for the VLTI interferometer. Using different baselines, they found that the inner regions (1−2 AU) of the disks are more crystalline compared to the outer regions (2−20 AU). Beside the fact that their sample is limited to 3 intermediate mass objects while we analyse a statistically significant TTs sample, direct comparison of their observations with ours is not straightforward. They do have spatial information, but only for the 10 μm spectral region, while we cover a larger spectral range. We, on the other hand, are observing the entire disk with Spitzer/IRS, with no direct spatial information. An ideal and challenging way to confront such kinds of interferometric data with IRS would be to repeat similar observations for TTs and even better, at wavelengths larger than 20 μm. This will ultimately require space-born interferometers because of the poor atmosphere transmission in the mid-IR. With such observations, however, we would then be able to constrain the crystalline fraction in the inner and outer regions of the disk more directly.

5.5. On the similarities with Solar System objects

Studies of Solar Sytem asteroids and comets show strong similarities with our results. First of all, laboratory studies of asteroidal and cometary solids have show that they contain very little ISM-like materials. The 81P/Wild 2 samples from the Stardust mission McKeegan et al. (2006), for example, show that this comet contains high-temperature silicates and oxide minerals. These authors conclude that such materials could not have been formed via annealing of presolar amorphous silicates in the Kuiper belt, and also that they could not have been formed from a single isotopic reservoir. Overall, this suggests that comet 81P/Wild 2 sampled different regions of the inner solar protoplanetary disk during its formation. One proposed transportation mechanism is the combination of winds associated with bipolar outflows. This hypothesis is also supported by laboratory measurements from Toppani et al. (2006) on condensation under high temperature, low-pressure conditions. Mg-rich silicates crystals can rapidly (~1 h at 4 × 10^{-3} bar) be produced from the gas phase through condensation, confirming the fact that crystalline grains can be produced even in bipolar outflows from evolved stars. In still further work on the 81P/Wild 2 Stardust mission, Zolensky et al. (2006), found large abundances of crystalline materials. Olivine is present in most of the studied particles, with grain sizes ranging between submicron-sized to over 10 μm, and it is concluded that some materials in the comet have seen temperatures possibly higher than 2000 K. Similar to McKeegan et al. (2006), large-scale radial transportation mechanisms inside the disk are required to match the derived mineralogy of the olivine samples. Similar results were found studying other solar system bodies, for exemple, comet Hale-Bopp. Spectroscopic studies of this object (Wooden et al. 1999; Wooden et al. 2000) revealed the presence of crystalline olivine, crystalline ortho-pyroxene and crystalline clino-pyroxene, in significant quantities.

All these results echo the *crystallinity paradox* we find in our Spitzer observations, in the sense that the disk dust content is far from being homogeneous, and even far from the simple picture with crystalline grains close to the central object and amorphous content in the outer regions.

6. Summary and conclusion

We have conducted in this paper a comprehensive statistical study of crystalline silicates in proto-planetary (class II) disks which was made possible thanks to the high sensitivity of the spectroscopic instrument IRS (5−35 μm) onboard the Spitzer Space Telescope. This unprecedented work is among the first statistical studies of crystalline silicates emission features over a large sample of young solar-analog stars (96 objects). We find the following results:

1. Crystallinity is not a marginal phenomenon in class II disks around young solar analogs, as more than 3/4 of the objects show at least one crystalline feature in the IRS spectra. Crystalline features emitting at wavelengths larger than 20 μm are in addition widely present: both the C23 and C28 complexes, produced by enstatite plus forsterite features, are present at a frequency larger than 50%.

2. The crystalline silicates revealed by the IRS spectra are essentially Mg-rich silicates (forsterite, enstatite), with a small contribution of CaMg-rich silicates (diopside). We find no evidence of Fe-rich silicates (marginal evidence for fayalite) nor troilite (FeS) in our spectra.
3. We find that the amorphous 10 μm feature is not correlated with the C23, C28 and 33.6 μm crystalline features, neither on the basis of the frequencies at which they are detected nor on the fluxes they emit. Crystalline features emitted at wavelengths larger than 20 μm are, on the other hand, correlated to each other (C23, C28 and 33.6 μm), based either on detection frequencies and band fluxes.
4. From previous results, we conclude that within the spectral range of the Spitzer/IRS instrument, we are probing essentially two independent dust populations (see the illustration in Fig. 14): a warm component, which is likely located close to the central object ($\leq$1 AU), emitting features in the 10 μm region, and a second component, located at larger radii ($\leq$10 AU) or deeper inside the disk; the latter cold component being responsible for the emission of both C23 and C28 complexes plus the 33.6 μm forsterite feature.
5. For a large majority of objects, the upper layers of the disks are populated essentially by micron-sized grains, suggesting that submicron grains are largely depleted in disks atmospheres. For the amorphous 10 μm feature, we find the known correlation between the shape and the strength of the feature used as a grain size proxy and showing that the grains are μm-sized or larger. We adapted this relationship to the C23 complex and find similar results for the crystalline grains producing this complex. We also noted that the grain size proxies for the 10 μm and C23 features are uncorrelated.
6. We find a correlation between the shape of the SED (F_{30}/F_{13}) and the grain size proxy for the 10 μm feature. We see rather small, warm amorphous silicates for flared disks and grains becoming larger as disks are flattening. This trend is almost reversed for the cold, C23 crystalline grains as small crystals are only found for flattened SEDs.
7. We identify an apparent *crystallinity paradox* since the cold crystalline features ($\lambda > 20$ μm) are much more frequently detected than the warm ones ($\lambda \sim 10$ μm). We show that crystalline features can be hidden by amorphous features, especially near $\lambda \simeq 10\,\mu$m, but this contrast effect is insufficient to explain the difference regarding the apparition frequencies of the C23 complex and the 11.3 μm forsterite feature, suggesting that the warm grain population is, on average, intrinsically more amorphous than the cold grain population.

We argue that our Spitzer spectroscopic observations of disks around young stars reveal ongoing dynamical processes in planet-forming regions of disks that future theoretical disk evolution and planet formation models will have to explain:

- some mechanisms must supply the upper layers of the disks with micron-sized grains that should otherwise grow and settle rapidly. Vertical turbulent diffusion, accompanied by grain-grain fragmentation, would be natural candidates;
- some mechanisms must act efficiently to remove the submicron-size grains from the regions which are optically thin at IRS wavelengths. Stellar winds and radiation pressure have been suggested as possible processes;
- and, some mechanisms are responsible for rendering the colder disks regions much more crystalline than the warmer zones (*crystallinity paradox*). If this result has to do with dust radial mixing, it teaches us that the mixing does not result in a disk with a homogenous grain composition, and that it must transport crystals efficiently into the "comet-forming regions".

Acknowledgements. The authors warmly thank Bram Acke for his help on the IDL routine to extract the crystalline features characteristics, Jérome Aléon and Matthieu Gounelle for sharing with us their precious knowledge of small solid Solar System bodies, and Joel Green for the rich discussions we had. We also thank the anonymous referee for the very useful comments that helped improving this study. It is also a pleasure to acknowledge fruitful discussions with the Grenoble FOST team members, as well as the participants to the ANR (Agence Nationale de la Recherche of France) project ANR-07-BLAN-0221. This research is partly supported by the *Programme National de Physique Stellaire* (PNPS).

References

Acke, B., & van den Ancker, M. E. 2004, A&A, 426, 151
Alcala, J. M., Krautter, J., Schmitt, J. H. M. M., et al. 1995, A&AS, 114, 109
Andrews, S. M., & Williams, J. P. 2007, ApJ, 659, 705
Bouwman, J., Meeus, G., de Koter, A., et al. 2001, A&A, 375, 950
Bouwman, J., Henning, T., Hillenbrand, L. A., et al. 2008, ApJ, 683, 479
Bouy, H., Huélamo, N., Pinte, C., et al. 2008, A&A, 486, 877
Brown, J. M., Blake, G. A., Dullemond, C. P., et al. 2007, ApJ, 664, L107
Chen, H., Grenfell, T. G., Myers, P. C., & Hughes, J. D. 1997, ApJ, 478, 295
Chihara, H., Koike, C., Tsuchiyama, A., Tachibana, S., & Sakamoto, D. 2002, A&A, 391, 267
Ciesla, F. J. 2009, Icarus, 200, 655
Crovisier, J., Leech, K., Bockelee-Morvan, D., et al. 1997, Science, 275, 1904
D'Alessio, P., Calvet, N., Hartmann, L., Franco-Hernández, R., & Servín, H. 2006, ApJ, 638, 314
Davoisne, C., Djouadi, Z., Leroux, H., et al. 2006, A&A, 448, L1
Desch, S. J., & Connolly, Jr., H. C. 2002, Meteoritics and Planetary Science, 37, 183
Dominik, C., Dullemond, C. P., Waters, L. B. F. M., & Walch, S. 2003, A&A, 398, 607
Dorschner, J., Begemann, B., Henning, T., Jaeger, C., & Mutschke, H. 1995, A&A, 300, 503
Dullemond, C. P., & Dominik, C. 2005, A&A, 434, 971
Dullemond, C. P., & Dominik, C. 2008, A&A, 487, 205
Evans, II, N. J., Allen, L. E., Blake, G. A., et al. 2003, PASP, 115, 965
Evans, N. J., Dunham, M. M., Jørgensen, J. K., et al. 2009, ApJS, 181, 321
Fabian, D., Henning, T., Jäger, C., et al. 2001, A&A, 378, 228
Fromang, S., & Nelson, R. P. 2009, A&A, 496, 597
Furlan, E., Hartmann, L., Calvet, N., et al. 2006, ApJS, 165, 568
Gail, H.-P. 1998, A&A, 332, 1099
Gail, H.-P. 2004, A&A, 413, 571
Geers, V. C. 2007, Ph.D. Thesis, Leiden Observatory, Leiden University, PO Box 9513, 2300 RA Leiden, The Netherlands
Geers, V. C., Augereau, J.-C., Pontoppidan, K. M., et al. 2006, A&A, 459, 545
Hallenbeck, S. L., Nuth, III, J. A., & Nelson, R. N. 2000, ApJ, 535, 247
Harker, D. E., & Desch, S. J. 2002, ApJ, 565, L109
Harker, D. E., Woodward, C. E., Wooden, D. H., Fisher, R. S., & Trujillo, C. A. 2007, Icarus, 190, 432
Herbig, G. H., & Bell, K. R. 1988, Third catalog of emission-line stars of the Orion population, ed. G. H. Herbig, & K. R. Bell
Honda, M., Kataza, H., Okamoto, Y. K., et al. 2003, ApJ, 585, L59
Honda, M., Kataza, H., Okamoto, Y. K., et al. 2006, ApJ, 646, 1024
Hughes, J., & Hartigan, P. 1992, AJ, 104, 680
Jaeger, C., Molster, F. J., Dorschner, J., et al. 1998, A&A, 339, 904
Keller, C., & Gail, H.-P. 2004, A&A, 415, 1177
Keller, L. P., Hony, S., Bradley, J. P., et al. 2002, Nature, 417, 148
Kessler-Silacci, J., Augereau, J.-C., Dullemond, C. P., et al. 2006, ApJ, 639, 275
Kessler-Silacci, J. E., Dullemond, C. P., Augereau, J.-C., et al. 2007, ApJ, 659, 680
Kimura, Y., Miyazaki, Y., Kumamoto, A., Saito, M., & Kaito, C. 2008, ApJ, 680, L89
Koike, C., Tsuchiyama, A., Shibai, H., et al. 2000, A&A, 363, 1115
Koike, C., Chihara, H., Tsuchiyama, A., et al. 2003, A&A, 399, 1101
Krautter, J., Wichmann, R., Schmitt, J. H. M. M., et al. 1997, A&AS, 123, 329
Lahuis, F., Kessler-Silacci, J. E., Evans, N. J., et al. 2006, c2d Spectroscopy Explanatory Supplement, Tech. rep., Pasadena, Spitzer Science Center

Lahuis, F., van Dishoeck, E. F., Blake, G. A., et al. 2007, ApJ, 665, 492
Laibe, G., Gonzalez, J.-F., Fouchet, L., & Maddison, S. T. 2008, A&A, 487, 265
Lawson, W. A., Feigelson, E. D., & Huenemoerder, D. P. 1996, MNRAS, 280, 1071
McKeegan, K. D., Aléon, J., Bradley, J., et al. 2006, Science, 314, 1724
Merín, B., Augereau, J.-C., van Dishoeck, E. F., et al. 2007, ApJ, 661, 361
Min, M., Hovenier, J. W., & de Koter, A. 2005, A&A, 432, 909
Min, M., Hovenier, J. W., Waters, L. B. F. M., & de Koter, A. 2008, A&A, 489, 135
Molster, F. J., Waters, L. B. F. M., & Tielens, A. G. G. M. 2002, A&A, 382, 222
Natta, A., Meyer, M. R., & Beckwith, S. V. W. 2000, ApJ, 534, 838
Natta, A., Testi, L., Calvet, N., et al. 2007, in Protostars and Planets V, ed. B. Reipurth, D. Jewitt, & K. Keil, 767
Nuth, J. A., & Johnson, N. M. 2006, Icarus, 180, 243
Oliveira, I., Merín, B., Pontoppidan, K. M., et al. 2009, ApJ, 691, 672
Padgett, D. L., Cieza, L., Stapelfeldt, K. R., et al. 2006, ApJ, 645, 1283
Pinte, C., Padgett, D. L., Ménard, F., et al. 2008, A&A, 489, 633
Press, W. H., Teukolsky, S. A., Vetterling, W. T., & Flannery, B. P. 1992, Numerical recipes in C. The art of scientific computing, ed. W. H. Press, S. A. Teukolsky, W. T. Vetterling, & B. P. Flannery
Przygodda, F., van Boekel, R., Àbrahàm, P., et al. 2003, A&A, 412, L43
Salyk, C., Pontoppidan, K. M., Blake, G. A., et al. 2008, ApJ, 676, L49
Sargent, B. A., Forrest, W. J., Tayrien, C., et al. 2009, ApJS, 182, 477
Savitzky, A., & Golay, M. J. E. 1964, Anal. Chem., 36, 1627
Servoin, J., & Piriou, B. 1973, Phys. Stat. Sol. (b), 55, 677
Sitko, M. L., Lynch, D. K., & Russell, R. W. 2000, AJ, 120, 2609
Sloan, G. C., Kraemer, K. E., Goebel, J. H., & Price, S. D. 2003, ApJ, 594, 483
Takeuchi, T., & Lin, D. N. C. 2003, ApJ, 593, 524
Toppani, A., Libourel, G., Robert, F., & Ghanbaja, J. 2006, Geochim. Cosmochim. Acta, 70, 5035
Valenti, J. A., Fallon, A. A., & Johns-Krull, C. M. 2003, ApJS, 147, 305
van Boekel, R., Waters, L. B. F. M., Dominik, C., et al. 2003, A&A, 400, L21
van Boekel, R., Min, M., Leinert, C., et al. 2004, Nature, 432, 479
van Boekel, R., Min, M., Waters, L. B. F. M., et al. 2005, A&A, 437, 189
Watson, D. M., Leisenring, J. M., Furlan, E., et al. 2009, ApJS, 180, 84
Wichmann, R., Krautter, J., Schmitt, J. H. M. M., et al. 1996, A&A, 312, 439
Wooden, D. H., Harker, D. E., Woodward, C. E., et al. 1999, ApJ, 517, 1034
Wooden, D. H., Butner, H. M., Harker, D. E., & Woodward, C. E. 2000, Icarus, 143, 126
Wooden, D., Desch, S., Harker, D., Gail, H.-P., & Keller, L. 2007, in Protostars and Planets V, ed. B. Reipurth, D. Jewitt, & K. Keil, 815
Zolensky, M. E., Zega, T. J., Yano, H., et al. 2006, Science, 314, 1735

Table 4. Characteristics of the observations.

Starname	RA (J2000)	Dec (J2000)	Class	SpT	AOR Key	Obs. date	Modules
Perseus							
RNO 15	03h27m47.68s	30d12m04.3s	TTs (II)	–	0005633280	2004-08-30	SL, SH, LH
LkHα 325	03h28m52.22s	30d45m05.5s	CTTs (II)	K2[a]	0015737600	2005-09-05	SL, LL
LkHα 270	03h29m17.66s	31d22m45.1s	TTs (II)	K2.5-K7	0005634048	2005-02-08	SL, SH, LH
LkHα 271	03h29m21.87s	31d15m36.3s	TTs (II)	K3-K5	0011827968	2005-02-10	SL, SH, LH
SSTc2dJ033036.0+303024	03h30m35.94s	30d30m24.4s	II	–	0015737600	2005-09-05	SL, LL
SSTc2dJ033037.0+303128	03h30m36.98s	30d31m27.7s	II	–	0015737600	2005-09-05	SL, LL
LkHα 326	03h30m44.05s	30d32m46.7s	TTs (II)	G-M0	0005634304	2005-02-10	SL, SH, LH
SSTc2dJ033052.5+305418	03h30m52.58s	30d54m18.1s	II	–	0015737088	2005-09-05	SL, LL
SSTc2dJ033241.7+311046	03h32m41.76s	31d10m46.6s	II	–	0015737344	2005-09-05	SL, LL
LkHα 327	03h33m30.41s	31d10m50.4s	TTs (II)	A9-K2	0005634560	2004-02-03	SL, SH, LH
SSTc2dJ033341.3+311341	03h33m41.30s	31d13m41.6s	II	–	0015736832	2005-09-05	SL, LL
BD+31 634	03h41m39.20s	31d36m10.3s	HAeBe (II)	A8V	0015736320	2005-09-05	SL, LL
SSTc2dJ034219.3+314327	03h42m19.31s	31d43m26.6s	II	–	0015736064	2005-09-05	SL, LL
IRAS 03406+3133	03h43m44.54s	31d43m09.1s	–	–	0015735296	2005-09-05	SL, LL
LkHα 330	03h45m48.29s	32d24m11.8s	CTTs (II)	G3	0005634816	2004-09-02	SL, SH, LH
IRAS 03446+3254	03h47m47.12s	33d04m03.4s	TTs (II)	–	0005635072	2004-09-29	SL, SH, LH
Taurus							
LkCa 8	04h24m57.08s	27d11m56.5s	CTTs (II)	M0	0009832960	2005-02-08	SH, LH
IQ Tau	04h29m51.56s	26d06m45.0s	WTTs (II)	M0-M0.5	0009832704	2005-02-09	SH, LH
FX Tau	04h30m29.62s	24d26m45.1s	C+WTTs (II)	M1-M4	0009832448	2005-02-10	SH, LH
V710 Tau	04h31m57.79s	18d21m36.3s	C+WTTs (II)	M0.5-M3	0005636608	2004-09-29	SH, LH
RX J0432.8+1735	04h32m53.23s	17d35m33.7s	TTs (II)	M2[b]	0015917824	2005-09-09	SL, LL
DN Tau	04h35m27.37s	24d14m58.8s	CTTs (II)	M0	0009831936	2005-02-10	SH, LH
CoKu Tau 3	04h35m40.94s	24d11m08.6s	CTTs (II)	M1	0009831936	2005-02-10	SH, LH
CoKu Tau 4	04h41m16.79s	28d40m00.5s	CTTs (II)	M1.5	0005637888	2004-09-02	SH, LH
RR Tau	05h39m30.52s	26d22m27.0s	HAeBe (II)	B8-A5	0005638400	2004-09-28	SL, SH, LH
Chamaleon							
SX Cha	10h55m59.74s	–77d24m39.9s	TTs (II)	M0.5	0005639424	2004-08-31	SH, LH
SY Cha	10h56m30.47s	–77d11m39.4s	TTs (II)	M0	0005639424	2004-08-31	SH, LH
TW Cha	10h59m01.10s	–77d22m40.80s	TTs (II)	K0-M0	0005639680	2004-09-01	SH, LH
B35	11h07m21.49s	–77d22m11.8s	CTTs (II)	M2	0005639680	2004-09-01	SH, LH
VW Cha	11h08m01.50s	–77d42m28.70s	CTTs (II)	K2-K7	0005639680	2004-09-01	SH, LH
Hn 9	11h09m18.16s	–76d30m29.2s	–	K4-M1[c]	0009831168	2005-02-10	SL, LL
VZ Cha	11h09m23.80s	–76d23m20.7s	TTs (II)	K6-K7	0005640448	2004-09-02	SH, LH
WX Cha	11h09m58.75s	–77d37m08.9s	TTs (II)	K7-M0	0005640192	2004-09-01	SH, LH
ISO-Cha237	11h10m11.44s	–76d35m29.2s	TTs (II)	M0	0005640448	2004-09-02	SL, LL
C7-11	11h10m38.01s	–77d32m39.9s	TTs (II)	K3	0005640192	2004-09-01	SH, LH
HM 27	11h10m49.62s	–77d17m51.7s	TTs (II)	K7	0005640192	2004-09-01	SH, LH
XX Cha	11h11m39.67s	–76d20m15.1s	TTs (II)	M1-M2	0005640448	2004-09-02	SH, LH
HD 98922	11h22m31.67s	–53d22m11.4s	HAeBe (II)	B9	0005640704	2004-01-04	SH, LH
HD 101412	11h39m44.46s	–60d10m27.7s	HAeBe (II)	B9.5	0005640960	2005-02-10	SL, SH, LH
T Cha	11h57m13.53s	–79d21m31.5s	TTs (II)	G2-K0	0005641216	2004-07-18	SH, LH
IRAS 12535-7623	12h57m11.78s	–76d40m11.5s	TTs (II)	M0	0011827456	2004-08-31	SH, LH

Table 4. continued.

Starname	RA (J2000)	Dec (J2000)	Class	SpT	AOR Key	Obs. date	Modules
ISO-ChaII 13	12h58m06.70s	–77d09m09.5s	BD (II)	–	0015918592	2005-09-13	SL, LL
RX J1301.0-7654	13h00m53.23s	–76d54m15.2s	–	K1[d]	0009830656	2005-03-12	SL, LL
Sz50	13h00m55.37s	–77d10m22.2s	TTs (II)	K7-M3	0011827456	2004-08-31	SH, LH
ISO-ChaII 54	13h00m59.20s	–77d14m02.7s	TTs (II)	K3	0015735040	2005-08-13	SL, SH, LL
Sz52	13h04m24.90s	–77d52m30.3s	–	–	0018215168	2006-07-03	SL, LL
Sz62	13h09m50.66s	–77d57m24.0s	–	M2[e]	0009830400	2005-03-12	SL, LL
Lupus							
HT Lup	15h45m12.87s	–34d17m30.6s	TTs (II)	K2	0005643264	2004-08-30	SL, SH, LH
GW Lup	15h46m44.68s	–34d30m35.4s	TTs (II)	M2-M4	0005643520	2004-08-30	SL, SH, LH
HM Lup	15h47m50.63s	–35d28m35.4s	TTs (II)	M4	0005643776	2004-08-30	SL, LL
Sz73	15h47m56.98s	–35d14m35.1s	TTs (II)	K2-M	0005644032	2004-08-30	SL, SH, LH
GQ Lup	15h49m12.10s	–35d39m05.0s	TTs (II)	K7-M0	0005644032	2004-08-30	SL, SH, LH
Sz76	15h49m30.74s	–35d49m51.4s	–	M1[f]	0015916288	2005-09-09	SL, LL
IM Lup	15h56m09.20s	–37d56m06.4s	TTs (II)	M0	0005644800	2004-08-30	SL, SH, LH
RU Lup	15h56m42.31s	–37d49m15.5s	CTTs (II)	K3-M0	0005644800	2004-08-30	SL, SH, LH
Sz84	15h58m02.50s	–37d36m02.8s	–	M5.5[g]	0005644288	2004-03-25	SL, LL
RY Lup	15h59m28.39s	–40d21m51.2s	TTs (II)	K0-K4	0005644544	2004-08-30	SL, SH, LH
EX Lup	16h03m05.50s	–40d18m24.9s	TTs (II)	M0	0005645056	2004-08-30	SL, SH, LH
RX J1603.2-3239	16h03m11.81s	–32d39m20.2s	TTs (II)	K7[g]	0015917312	2005-09-09	SL, LL
Sz96	16h08m12.62s	–39d08m33.4s	–	M1.5[f]	0016755200	2006-03-15	SL, LL
Sz102	16h08m29.70s	–39d03m11.2s	TTs (II)	M0	0009407488	2004-03-25	SL, SH, LH
SSTc2d J161159.8-382338	16h11m59.81s	–38d23m37.5s	II	–	0015737856	2005-08-14	SL, LL
RX J1615.3-3255	16h15m20.23s	–32d55m05.1s	TTs (II)	K5[h]	0015916800	2005-09-09	SL, LL
Ophiuchus							
AS 205	16h11m31.35s	–18d38m26.1s	TTs (II)	K5	0005646080	2004-08-28	SL, SH, LH
Haro 1-1	16h21m34.69s	–26d12m27.0s	CTTs (II)	K5-K7	0009833472	2005-03-12	SL, SH, LH
SSTc2d J162148.5-234027	16h21m48.49s	–23d40m27.4s	II	–	0015920897	2006-03-15	SL, LL
SSTc2d J162221.0-230403	16h22m21.01s	–23d04m02.6s	I	–	0015920897	2006-03-15	SL, LL
SSTc2d J162245.4-243124	16h22m45.40s	–24d31m23.9s	II	–	0015920641	2006-03-15	SL, LL
SSTc2d J162332.8-225847	16h23m32.85s	–22d58m46.9s	II	–	0015920641	2006-03-15	SL, LL
Haro 1-4	16h25m10.51s	–23d19m14.5s	TTs (II)	K4-K6	0009833216	2005-03-12	SH, LH
VSSG1	16h26m18.86s	–24d28m19.7s	TTs (II)	–	0005647616	2004-08-28	SH, LH
DoAr 24E	16h26m23.38s	–24d21m00.1s	TTs (II)	K0-K1	0005647616	2004-08-28	SH, LH
DoAr 25	16h26m23.68s	–24d43m14.00s	TTs (II)	K5[i]	0012663808	2005-08-12	SH, LH
GY23	16h26m24.06s	–24d24m48.1s	TTs (II)	K5-M2[j]	0005647616	2004-08-28	SH, LH
SR 21	16h27m10.28s	–24d19m12.5s	TTs (II)	F4-G2.5	0005647616	2004-08-28	SH, LH
SSTc2d J162715.1-245139	16h27m15.14s	–24d51m38.9s	II	–	0016754688	2006-03-15	SL, LL
SR 9	16h27m40.27s	–24d22m04.0s	TTs (II)	K5-M2	0012027392	2004-09-02	SH, LH
SSTc2d J162816.7-240514	16h28m16.73s	–24d05m14.3s	II	–	0016754944	2006-03-15	SL, LL
V853Oph	16h28m45.28s	–24d28m19.0s	TTs (II)	M1.5	0012408576	2005-03-12	SH, LH
ROX42C	16h31m15.75s	–24d34m02.1s	TTs (II)	K4-K6	0006369792	2005-03-12	SH, LH
ROX43A	16h31m20.13s	–24d30m05.1s	TTs (II)	G0	0015914496	2005-09-09	SH, LH
IRS60	16h31m30.89s	–24d24m39.7s	–	–	0006370048	2005-09-09	SH, LH
Haro 1-16	16h31m33.47s	–24d27m37.1s	TTs (II)	K2-K3	0012664064	2005-09-09	SH, LH

Table 4. continued.

Starname	RA (J2000)	Dec (J2000)	Class	SpT	AOR Key	Obs. date	Modules
Haro 1-17	16h32m21.94s	–24d42m14.7s	TTs (II)	M2.5	0011827712	2004-08-29	SL, SH, LH
RNO 90	16h34m09.20s	–15d48m16.80s	TTs (II)	G5	0005650432	2004-08-28	SL, SH, LH
Wa Oph 6	16h48m45.63s	–14d16m35.96s	TTs (II)	K7	0005650688	2006-03-15	SL, SH, LH
V1121 Oph	16h49m15.31s	–14d22m08.6s	CTTs (II)	K5	0005650688	2006-03-15	SL, SH, LH
HD 163296	17h56m21.29s	–21d57m21.9s	HAeBe (II)	A0-A2	0005650944	2004-08-28	SH, LH
Serpens							
VV Ser	18h28m47.86s	0d08m39.8s	HAeBe (II)	B1-A3	0005651200	2004-09-01	SL, SH, LH
SSTc2dJ182850.2+00950	18h28m50.21s	0d09m49.6s	II	M2[k]	0013461505	2006-04-21	SL, LL
SSTc2dJ182900.9+02931	18h29m00.90s	0d29m31.5s	II	–	0013210112	2005-04-17	SL, SH, LL
SSTc2dJ182901.2+02933	18h29m01.20s	0d29m33.2s	II	M0.5[k]	0013461505	2006-04-21	SL, LL
SSTc2dJ182901.8+02954	18h29m01.80s	0d29m54.3s	II	K7[k]	0013210112	2005-04-17	SL, SH, LL
SSTc2dJ182909.8+03446	18h29m09.80s	0d34m45.8s	–	M5	0013210624	2005-04-14	SL, SH, LL
SSTc2dJ182928.2+02257	18h29m28.24s	–0d22m57.4s	II	–	0013210368	2005-04-14	SL, SH, LL
EC69	18h29m54.35s	1d15m01.8s	II	–	0009407232	2004-03-27	SL, LL
EC82	18h29m56.89s	1d14m46.5s	TTs (II)	M0	0009407232	2004-03-27	SL, SH, LH
EC90	18h29m57.75s	1d14m05.9s	TTs (II)	–	0009828352	2004-09-01	SL, SH, LH
EC92	18h29m57.88s	1d12m51.6s	TTs (II)	K7-M2	0009407232	2004-03-27	SL, SH, LH
CK4	18h29m58.21s	1d15m21.7s	TTs (II)	K3	0009407232	2004-03-27	SL, SH, LH
LkHα 348	18h34m12.65s	–0d26m21.7s	TTs (II)	F6	0009831424	2006-04-16	SL,SH, LH
BF Ori	05h37m13.26s	–6d35m00.6s	HAeBe (II)	A5-F6	0005638144	2004-10-03	SL, SH, LH
IRAS 08267-3336	08h28m40.70s	–33d46m22.3s	TTs (II)	K2-K3	0005639168	2004-11-11	SL, SH, LH
HD 135344	15h15m48.44s	–37d09m16.0s	HAeBe (II)	A0-F4	0005657088	2004-08-08	SH, LH

Where reference for spectral type is not indicated, it comes from Lahuis et al. (2007), the third paper in the series of four c2d articles on IRS observations of TTauri stars. a) Herbig & Bell (1988); b) Wichmann et al. (1996); c) Lawson et al. (1996); d) Alcala et al. (1995); e) Hughes & Hartigan (1992); f) Chen et al. (1997); g) Krautter et al. (1997); h) Padgett et al. (2006); i) Andrews & Williams (2007); j) Kessler-Silacci et al. (2006); k) Oliveira et al. (2009).

Table 5. Signal-to-noise ratios for detections of crystalline silicate features, amorphous silicate 10 μm feature and silica.

Starname	9.2	Amorphous 10.0	11.3	12.5	16.2	21.6	C23	25.0	C28	33.6	$S_{11.3}/S_{9.8}$	$S^{10\,\mu m}_{Peak}$	S_{24}/S_{23}	$S^{23\,\mu m}_{Peak}$	F_{30}/F_{13}
Perseus															
RNO 15	–	871	–	–	–	–	–	–	–	–	0.92	1.45	–	–	1.13
LkHα 325	39	599	–	–	–	–	35	–	39	40	0.98	1.51	–	–	1.10
LkHα 270	22	109	–	–	–	–	108	–	–	–	1.01	1.11	0.51	9.83	1.59
LkHα 271	–	106	–	13	–	–	–	–	–	–	0.98	1.26	–	–	2.54
SSTc2d J033036.0+303024	192	1136	–	36	86	–	186	–	162	195	1.05	1.94	0.90	1.19	1.22
SSTc2d J033037.0+303128	–	330	–	–	–	–	–	–	33	–	0.99	1.32	–	–	0.97
LkHα 326	43	242	–	39	94	47	101	90	140	–	1.01	1.19	1.02	1.09	2.88
SSTc2d J033052.5+305418	–	307	–	8	–	–	14	10	22	–	0.97	1.71	0.85	1.18	1.60
SSTc2d J033241.7+311046	–	302	–	–	–	62	36	–	81	–	0.94	1.65	1.30	1.30	1.55
LkHα 327	–	105	–	19	–	–	141	–	–	198	1.06	1.12	0.22	6.60	1.23
SSTc2d J033341.3+311341	–	–	45	25	–	–	35	–	60	–	–	–	0.98	1.06	2.01
BD+31 634	–	421	–	–	93	–	69	–	–	–	–	–	–	–	2.82
SSTc2d J034219.3+314327	–	171	–	8	–	–	21	–	36	–	1.05	1.50	0.93	1.12	1.44
IRAS 03406+3133	–	301	–	34	–	–	87	55	72	88	1.08	1.49	0.77	1.33	1.36
LkHα 330	–	247	57^{PAHs}	–	–	–	–	–	–	–	0.99	1.32	–	–	11.74
IRAS 03446+3254	–	–	–	–	34	–	–	5	–	–	–	–	–	–	3.21
Taurus															
LkCa 8	–	–	–	–	–	–	154	64	–	–	–	–	0.92	1.73	2.28
IQ Tau	–	–	–	–	–	–	–	–	97	–	–	–	–	–	1.63
FX Tau	–	–	–	–	75	–	116	–	–	–	–	–	0.46	6.67	1.87
V710 Tau	58	293	–	–	28	35	23	–	27	–	0.96	1.35	0.99	1.05	1.41
RX J0432.8+1735	–	–	–	–	–	–	4	–	–	–	–	–	0.95	1.23	1.57
DN Tau	–	–	–	79	–	–	–	–	–	–	–	–	–	–	1.77
CoKu Tau 3	–	–	–	–	50	–	–	–	–	–	–	–	–	–	1.05
CoKu Tau 4	–	72	–	–	–	–	–	–	–	164	0.98	1.26	–	–	16.96
RR Tau	–	–	175	63	–	–	82	–	56	99	–	–	–	–	1.69
Chamaleon															
SX Cha	–	683	–	–	–	–	227	–	122	–	0.86	1.68	0.85	2.41	1.72
SY Cha	–	–	230	–	–	–	216	–	228	–	–	–	0.50	6.51	2.16
TW Cha	–	349	–	–	–	–	18	17	17	–	0.73	2.81	0.69	1.56	2.07
B35	–	96	8	10	–	–	15	–	–	15	0.92	1.52	1.00	1.06	2.39
VW Cha	–	511	–	20	42	82	47	34	75	88	0.96	1.59	0.94	1.07	2.08
Hn 9	–	395	–	–	–	–	26	10	22	31	0.95	1.57	0.94	1.09	1.54
VZ Cha	–	259	–	–	–	21	16	–	18	–	0.94	1.40	0.71	1.52	1.03
WX Cha	–	444	–	–	21	–	27	24	14	–	0.93	1.64	0.70	1.55	0.99
ISO-Cha237	–	123	12	–	–	–	–	–	–	–	0.94	1.38	–	–	1.09
C7-11	31	203	–	7	–	–	21	14	25	58	1.04	1.43	0.98	1.04	1.51
HM 27	–	339	–	–	–	41	101	–	–	–	0.85	1.60	0.96	1.14	2.03
XX Cha	45	230	–	16	–	–	26	–	27	–	0.92	1.46	0.97	1.06	1.70
HD 98922	–	–	191	46	–	–	260	–	–	103	–	–	–	–	0.70
HD 101412	36	409	–	–	–	–	137	–	–	–	–	–	–	–	0.92
T Cha	–	–	27^{PAHs}	–	–	–	–	–	–	–	–	–	–	–	8.26

Table 5. continued.

Starname	9.2	Amorphous 10.0	11.3	12.5	16.2	21.6	C23	25.0	C28	33.6	$S_{11.3}/S_{9.8}$	$S^{10\,\mu m}_{Peak}$	S_{24}/S_{23}	$S^{23\,\mu m}_{Peak}$	F_{30}/F_{13}
IRAS 12535-7623	–	438	–	–	16	–	23	11	23	13	0.95	1.75	0.69	1.47	1.06
ISO-ChaII 13	–	–	43	5	–	–	57	–	55	33	–	–	0.98	1.20	0.84
RX J1301.0-7654	–	806	–	–	–	70	66	48	25	–	0.84	1.87	0.89	1.40	1.62
Sz50	–	108	–	–	24	57	44	–	27	–	0.99	1.28	0.98	1.09	2.31
ISO-ChaII 54	–	–	171	–	69	–	258	–	371	409	–	–	0.94	1.21	2.54
Sz52	–	147	–	27	–	–	81	36	43	65	0.97	1.47	0.83	1.28	1.22
Sz62	–	171	–	27	–	17	13	14	33	–	1.08	1.51	0.93	1.14	1.17
Lupus															
HT Lup	–	699	–	–	–	–	–	–	–	–	0.96	1.38	–	–	1.53
GW Lup	–	145	–	4	–	–	13	11	–	26	0.90	1.43	0.92	1.27	1.56
HM Lup	–	313	–	–	–	–	16	–	–	–	0.88	1.70	0.97	1.04	1.78
Sz73	–	443	–	9	73	–	46	–	71	–	0.98	1.34	0.97	1.04	2.30
GQ Lup	31	360	–	–	–	–	20	23	34	–	0.96	1.31	0.97	1.04	2.04
Sz76	–	83	–	–	4	–	4	3	8	–	0.82	1.58	0.95	1.08	2.31
IM Lup	65	803	–	–	–	–	34	–	42	–	0.89	1.64	0.93	1.17	1.85
RU Lup	–	446	–	25	–	–	95	–	157	94	0.98	1.54	0.94	1.07	1.94
RY Lup	–	1690	–	–	–	–	52	–	78	–	0.69	2.82	0.99	1.09	3.92
EX Lup	–	856	–	–	–	–	79	55	–	59	0.76	1.89	0.74	1.41	1.56
RX J1603.2-3239	–	–	–	–	–	–	14	–	–	14	–	–	0.42	2.39	2.74
Sz96	–	849	–	–	25	33	64	–	72	107	0.84	2.34	0.93	1.13	1.61
Sz102	–	231	–	34	–	–	–	–	–	–	0.90	2.02	–	–	3.95
SSTc2dJ161159.8-382338	–	187	–	3	21	–	24	–	24	46	0.92	2.26	0.94	1.15	1.81
RX J1615.3-3255	16	226	–	6	9	–	13	–	18	–	1.14	3.06	1.03	1.08	6.52
Ophiuchus															
AS 205	–	796	–	–	–	–	–	–	–	–	0.90	1.60	–	–	1.76
Haro 1-1	–	551	–	–	–	–	20	–	39	–	0.72	2.87	1.00	1.02	4.70
SSTc2dJ162148.5-234027	–	253	37	18	–	–	62	26	52	189	1.02	1.63	0.96	1.10	3.77
SSTc2dJ162221.0-230403	–	121	–	1	–	–	–	–	–	–	0.82	2.66	–	–	5.69
SSTc2dJ162245.4-243124	–	408	–	–	87	–	103	–	–	83	1.03	1.81	0.97	1.06	3.20
SSTc2dJ162332.8-225847	–	193	–	17	14	–	12	–	–	–	1.00	2.49	1.00	1.19	1.77
Haro 1-4	–	304	–	8	–	–	–	–	–	505	1.05	1.85	–	–	2.44
VSSG1	–	–	–	12	–	–	37	26	40	–	–	–	0.83	1.21	1.06
DoAr 24E	–	–	100	–	23	–	20	–	37	–	–	–	0.96	1.09	1.92
DoAr25	–	–	84	–	–	–	86	–	103	258	–	–	0.93	1.04	3.31
GY23	–	–	81	–	41	–	23	8	49	–	–	–	0.84	1.20	1.01
SR 21	–	–	103[PAHs]	19	–	–	–	–	–	–	–	–	–	–	10.85
SSTc2dJ162715.1-245139	–	172	22	–	–	–	39	–	34	–	0.86	2.04	0.96	1.08	3.98
SR 9	–	715	–	–	–	–	17	–	39	32	0.77	2.53	0.84	1.22	2.66
SSTc2dJ162816.7-240514	19	–	83	–	13	–	69	–	54	63	–	–	0.93	1.15	1.19
V853Oph	–	–	–	–	–	–	78	–	80	–	–	–	0.99	1.06	1.69
ROX42C	130	278	–	25	57	–	76	–	89	–	0.95	1.48	0.97	1.07	1.90
ROX43A	175	2574	–	–	223	–	307	–	306	274	0.87	2.65	0.92	1.16	1.68
IRS60	–	405	–	–	–	–	26	3	35	86	0.98	1.44	0.98	1.07	1.69
Haro 1-16	–	1248	–	–	–	–	35	–	63	–	0.72	3.11	0.89	1.13	4.30

Table 5. continued.

Starname	9.2	Amorphous 10.0	11.3	12.5	16.2	21.6	C23	25.0	C28	33.6	$S_{11.3}/S_{9.8}$	$S_{\rm Peak}^{10\ \mu{\rm m}}$	S_{24}/S_{23}	$S_{\rm Peak}^{23\ \mu{\rm m}}$	F_{30}/F_{13}
Haro 1-17	55	374	–	–	–	–	21	–	20	25	0.98	1.55	0.88	1.19	1.96
RNO 90	–	520	–	–	–	–	39	40	–	–	0.92	1.47	0.79	1.31	1.75
Wa Oph 6	64	374	132	41	–	–	73	–	90	–	1.04	1.23	0.98	1.05	1.66
V1121 Oph	–	2663	–	–	–	–	177	–	161	–	0.85	2.23	1.02	1.20	1.87
HD 163296	–	–	278	32	–	–	186	–	–	56	–	–	–	–	1.56
Serpens															
VV Ser	–	659	–	–	–	–	–	–	–	–	–	–	–	–	0.76
SSTc2d J182850.2+00950	–	379	–	–	–	–	41	54	50	–	0.90	1.67	0.86	1.38	1.85
SSTc2d J182900.9+02931	–	313	–	–	–	–	25	16	39	34	0.98	1.27	0.89	1.15	1.75
SSTc2d J182901.2+02933	–	–	26	15	19	–	10	–	30	–	–	–	1.03	1.07	1.45
SSTc2d J182901.8+02954	–	–	18	–	–	32	18	9	43	40	–	–	0.90	1.11	1.46
SSTc2d J182909.8+03446	–	852	–	–	–	–	–	–	–	–	0.92	1.83	–	–	0.78
SSTc2d J182928.2+02257	141	1136	–	–	–	–	54	–	108	–	1.21	1.71	1.01	1.08	1.14
EC82	–	2618	–	–	–	–	–	–	–	–	0.73	3.29	–	–	3.33
EC90	46	–	–	–	113	–	193	–	–	148	–	–	0.97	1.21	1.61
CK4	–	305	–	–	–	–	–	–	–	–	0.92	1.50	–	–	2.47
LkHα 348	–	475	–	–	–	–	–	–	–	–	1.03	1.24	–	–	0.66
BF Ori	–	2113	–	–	57	–	–	–	22	26	–	–	–	–	0.84
IRAS 08267-3336	–	598	–	–	–	–	–	–	–	–	–	–	–	–	3.12
HD 135344	–	–	304	–	–	–	–	–	–	–	–	–	–	–	9.88

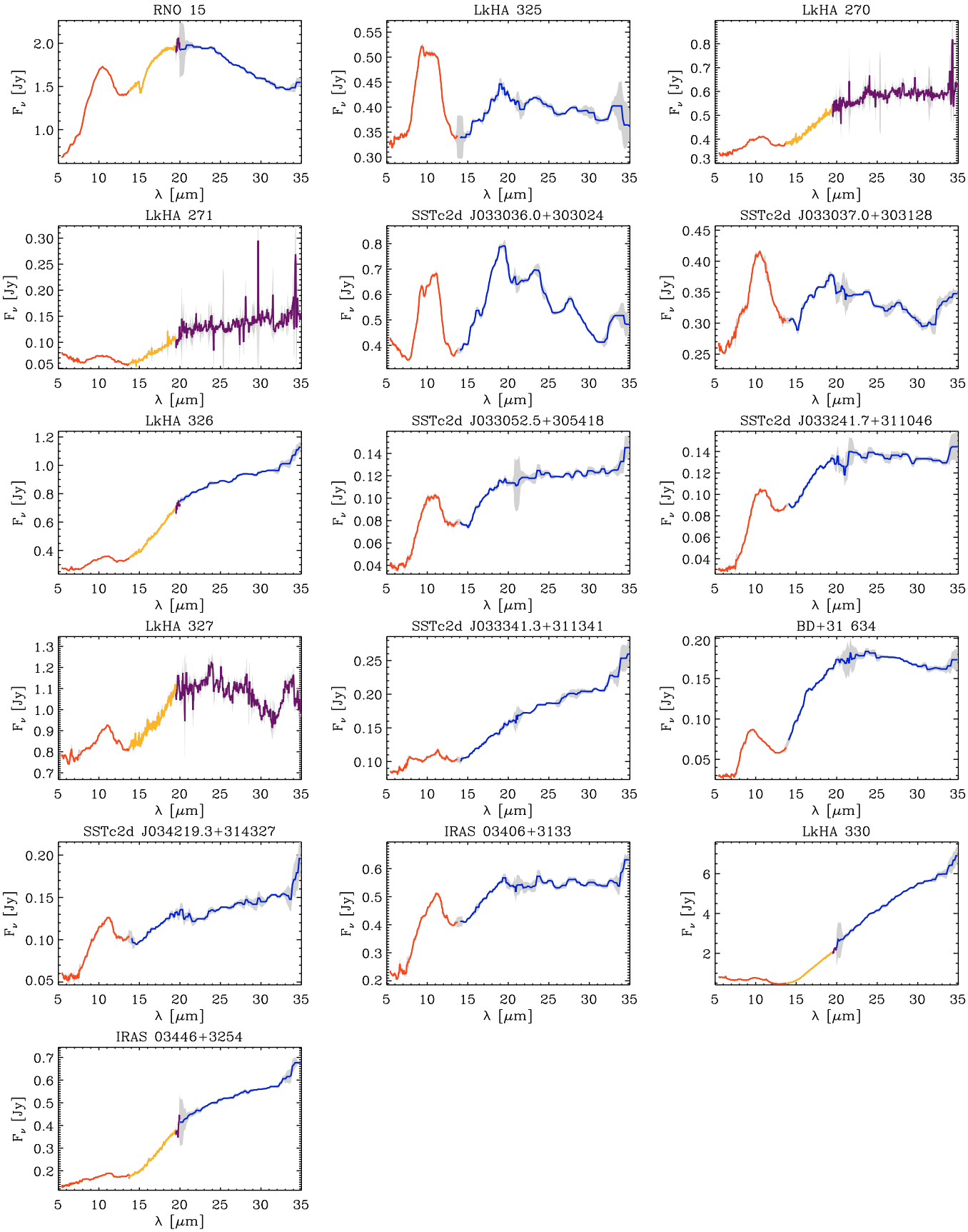

Fig. 15. Spitzer/IRS spectra of young stars in the Perseus cloud, in units of Jy. Gray areas correspond to 3-σ uncertainties as estimated in Sect. 2.4. Sources are sorted by increasing Right Ascension. Red color is for SL module, orange for SH, blue for LL and dark purple for LH.

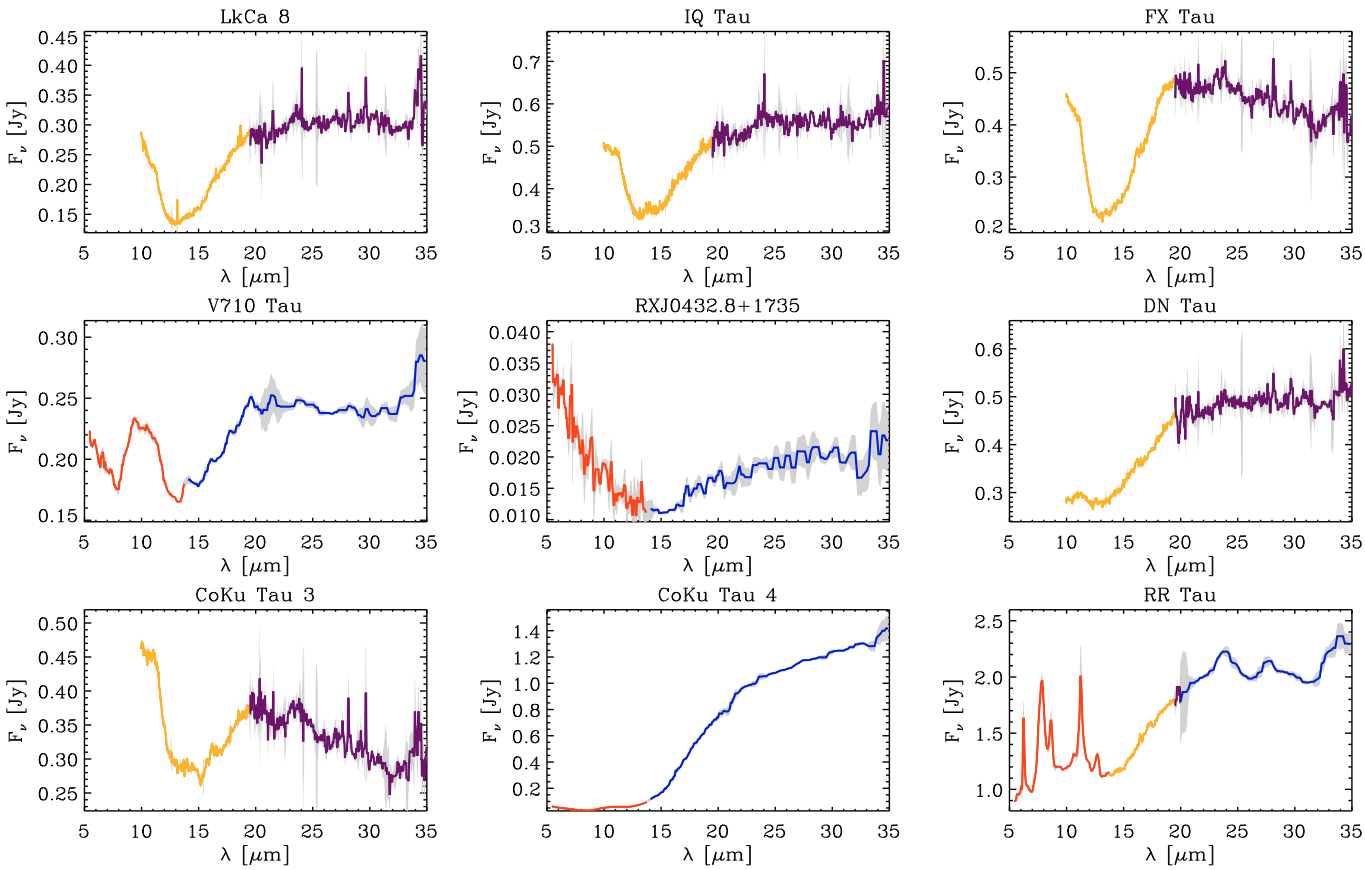

Fig. 16. Same as Fig. 15 but for the Taurus star sample.

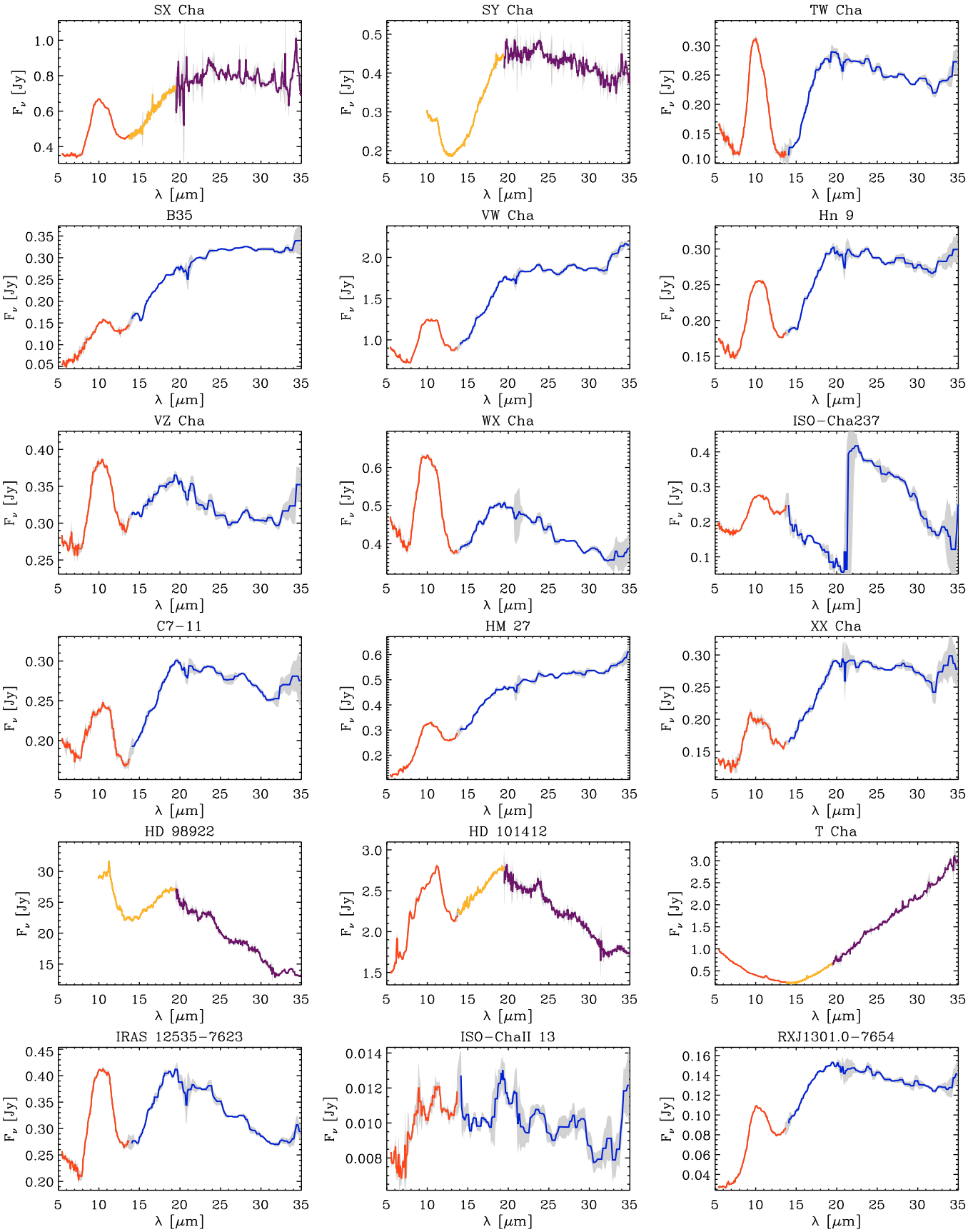

Fig. 17. Same as Fig. 15 but for the Chamaleon star sample.

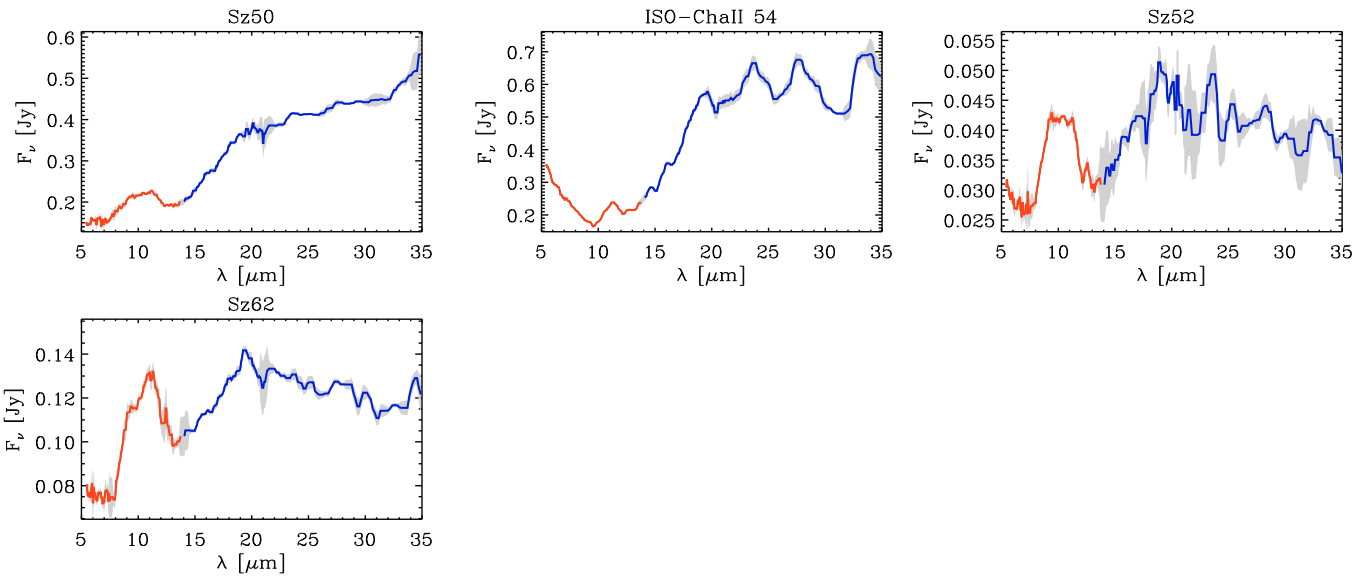

Fig. 18. Spitzer/IRS spectra for the Chamaleon sample: continued.

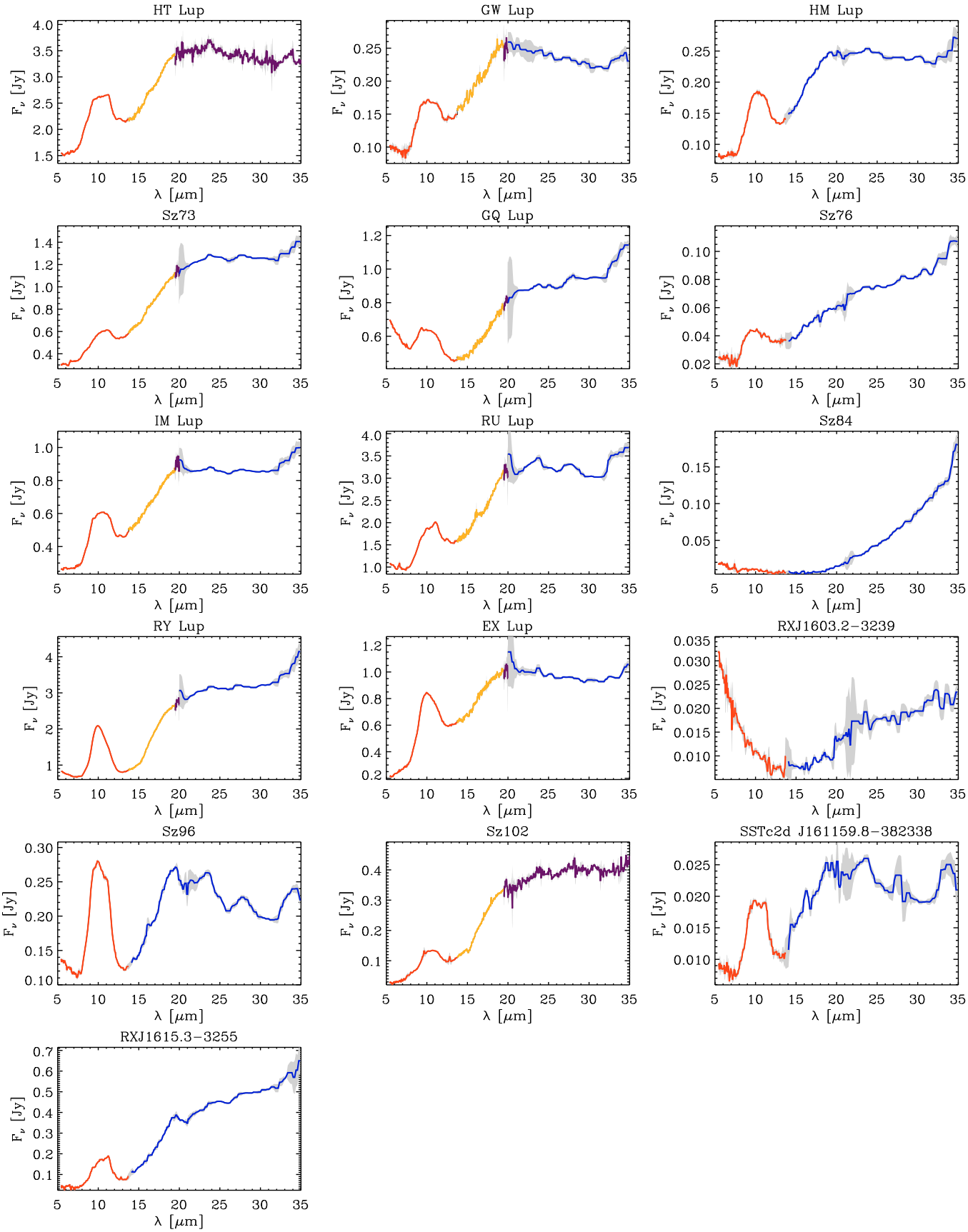

Fig. 19. Same as Fig. 15 but for the Lupus star sample.

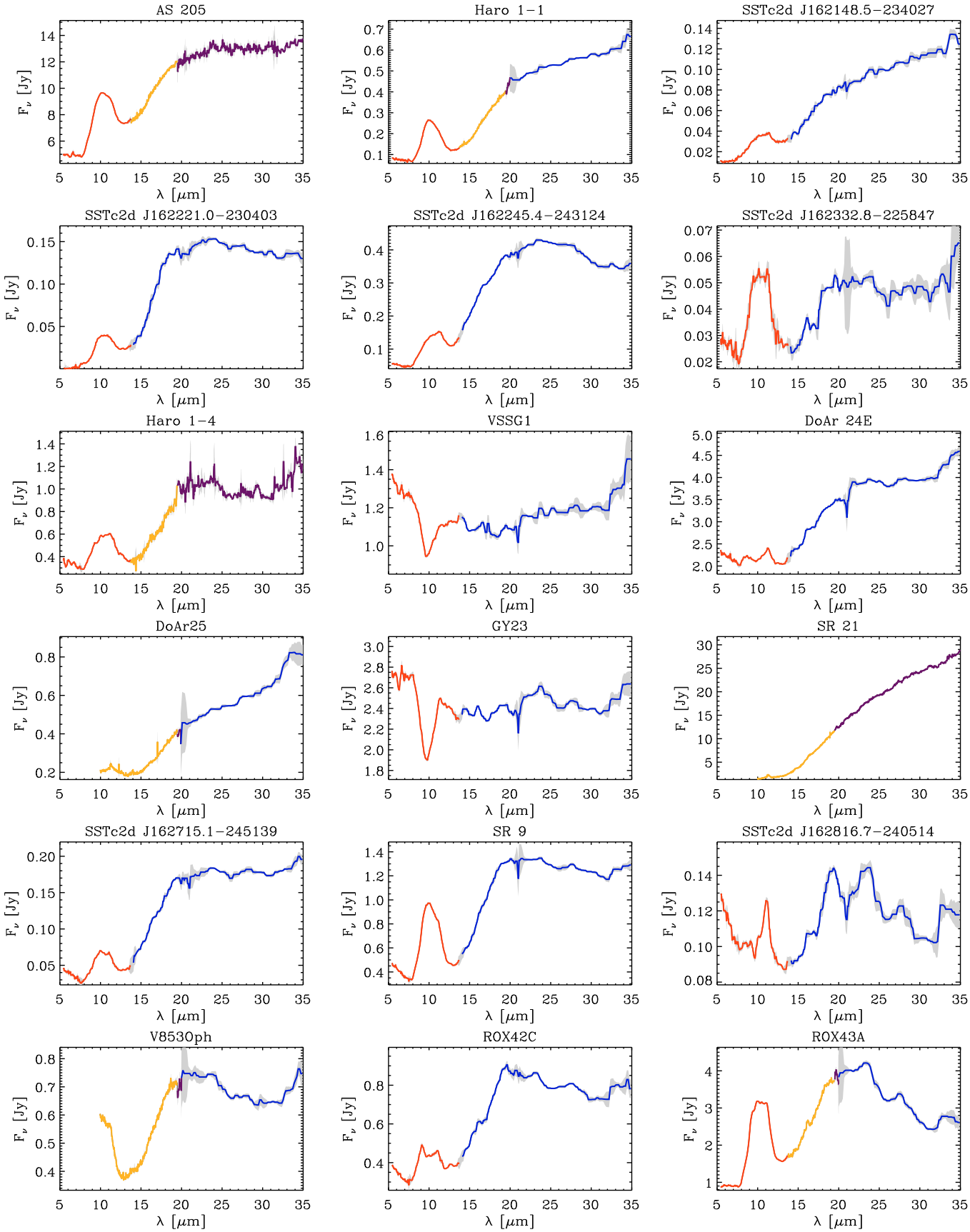

Fig. 20. Same as Fig. 15 but for the Ophiuchus star sample.

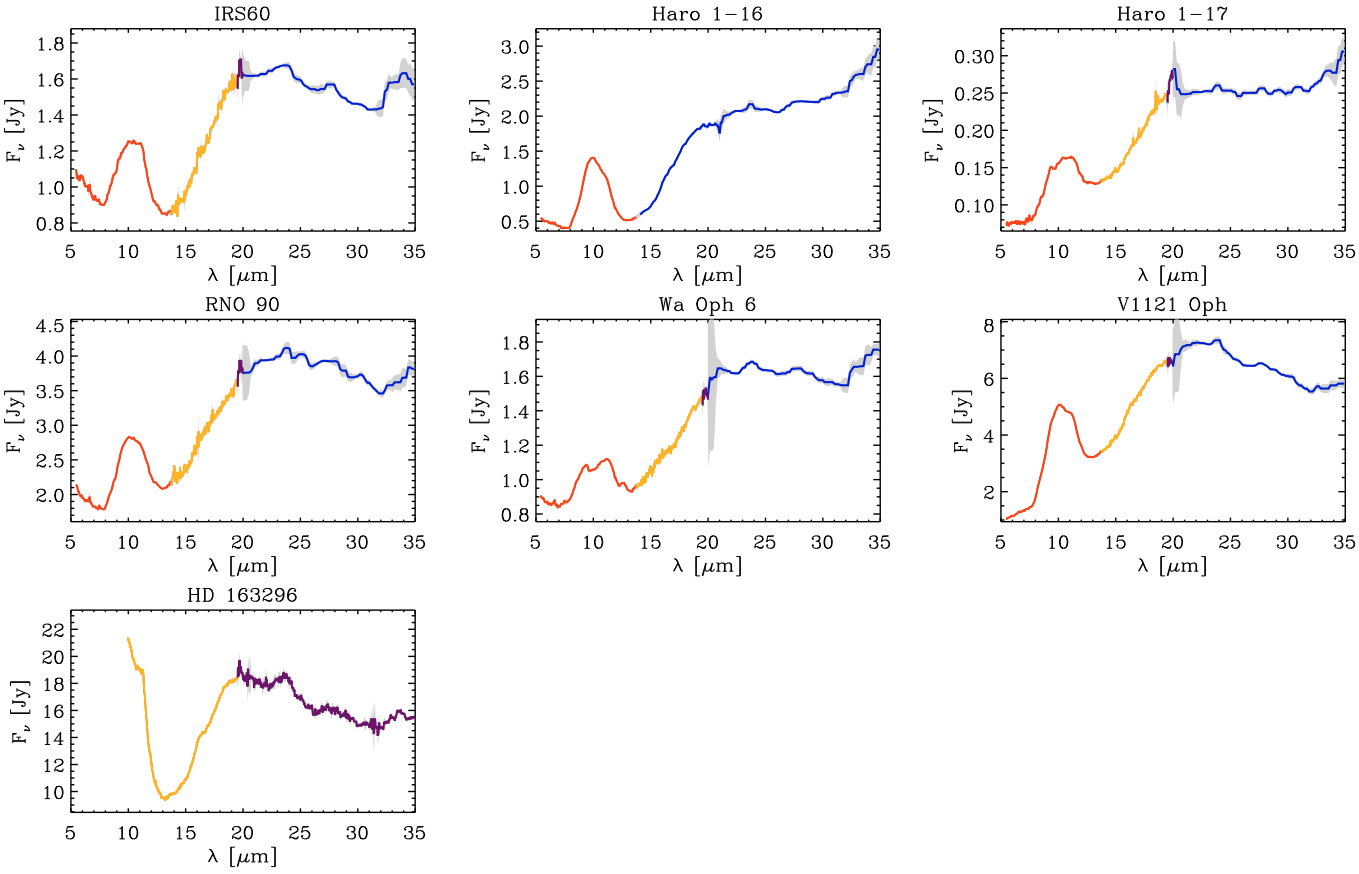

Fig. 21. Spitzer/IRS spectra for the Ophiuchus sample: continued.

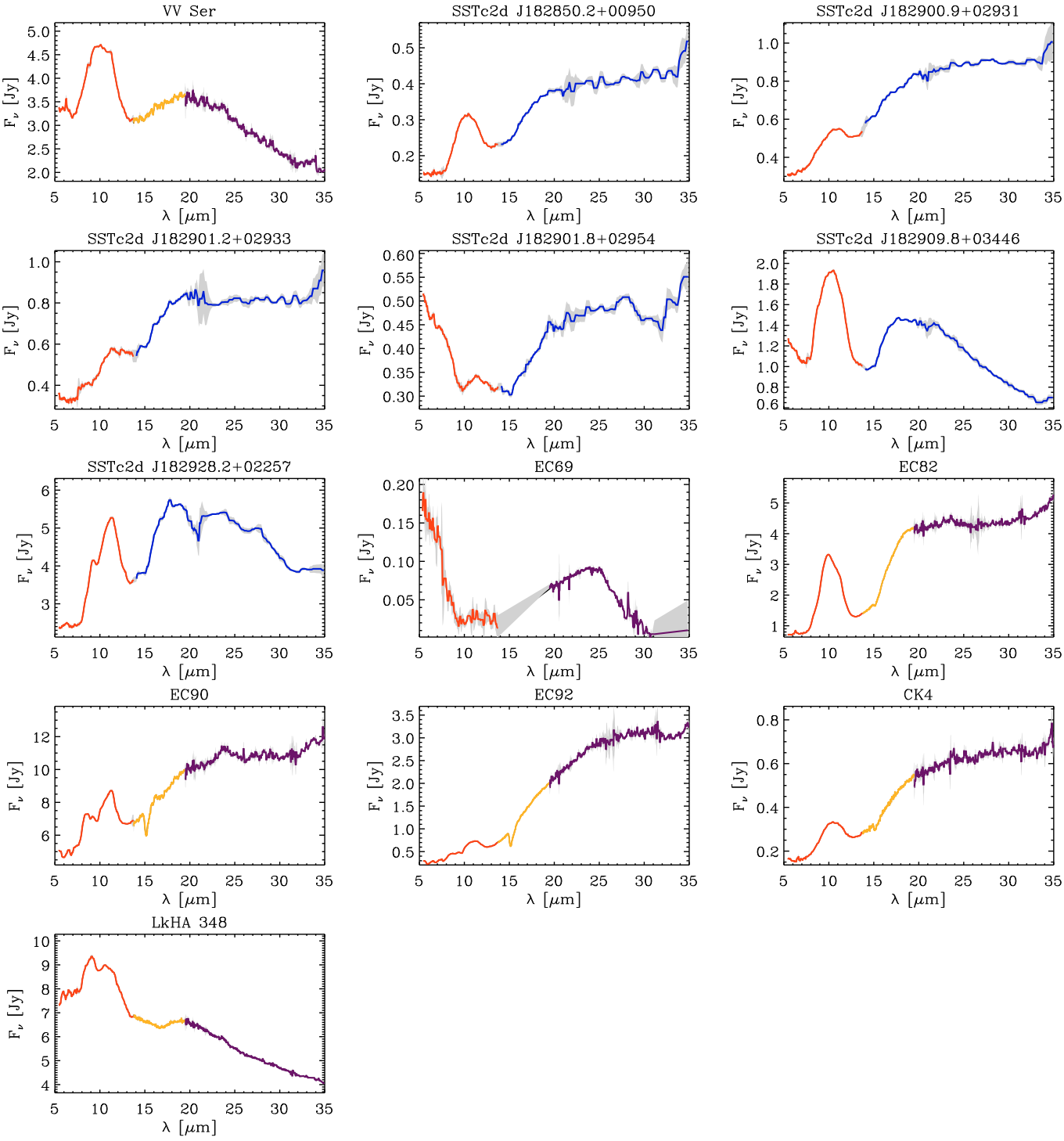

Fig. 22. Same as Fig. 15 but for the Serpens star sample.

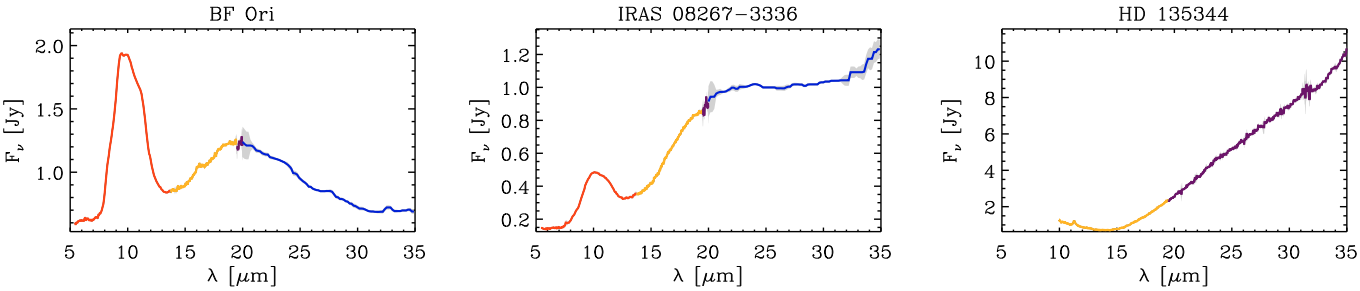

Fig. 23. Same as Fig. 15 but for the 3 isolated stars in our sample.

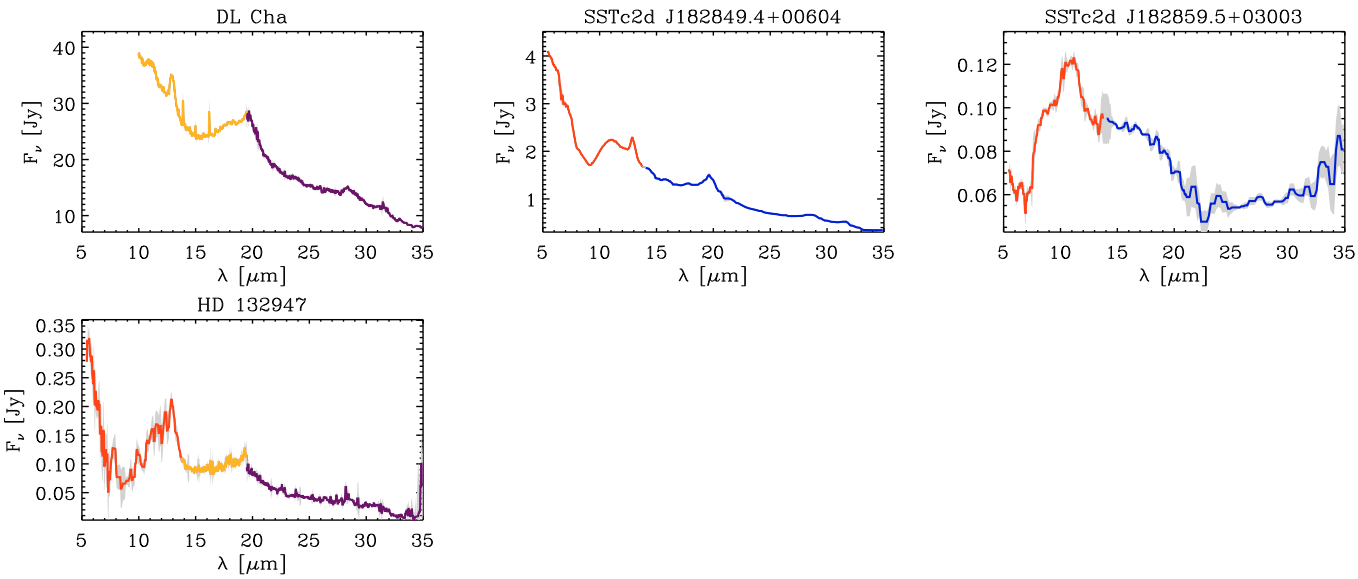

Fig. 24. Same as Fig. 15 but for the 4 objects with spectra similar to C-rich and O-rich AGB stars.